

Splitting of ScS waves due to lowermost mantle anisotropy: Practical challenges and new global measurements

Jonathan Wolf¹ and Maureen Long¹

¹Department of Earth and Planetary Sciences, Yale University

April 23, 2024

Abstract

Many regions of the Earth’s mantle are seismically anisotropic, including portions of the lowermost mantle, which may indicate deformation due to convective flow. The splitting of ScS phases, which reflect once off the core-mantle boundary (CMB), is commonly measured to identify lowermost mantle anisotropy, although some challenges exist. Here, we use global wavefield simulations to evaluate commonly used approaches to inferring a lowermost mantle contribution to ScS splitting. We show that due to effects of the CMB reflection, only the epicentral distance range between 60° and 70° is appropriate for ScS splitting measurements. For this distance range, splitting is diagnostic of deep mantle anisotropy if no upper mantle anisotropy is present; however, if ScS is also split due to upper mantle anisotropy, the reliable diagnosis of deep mantle anisotropy is challenging. Moreover, even in the case of a homogeneously anisotropic deep mantle region sampled from a single azimuth by multiple ScS waves with different source polarizations (in absence of upper mantle anisotropy), different apparent fast directions are produced. We suggest that ScS splitting should only be measured at “null” stations and conduct such an analysis worldwide. Our results indicate that seismic anisotropy is globally widespread in the deep mantle.

ScS shear-wave splitting in the lowermost mantle: Practical challenges and new global measurements

Jonathan Wolf *, Maureen D Long ¹

¹Department of Earth and Planetary Sciences, Yale University, New Haven, CT, USA

Author contributions: *Conceptualization*: Jonathan Wolf, Maureen Long. *Methodology*: Jonathan Wolf. *Software*: Jonathan Wolf. *Formal Analysis*: Jonathan Wolf. *Investigation*: Jonathan Wolf. *Writing - Original draft*: Jonathan Wolf. *Writing - Review & Editing*: Jonathan Wolf, Maureen Long. *Visualization*: Jonathan Wolf. *Supervision*: Maureen Long.

Abstract Many regions of the Earth’s mantle are seismically anisotropic, including portions of the lowermost mantle, which may indicate deformation due to convective flow. The splitting of ScS phases, which reflect once off the core-mantle boundary (CMB), is commonly measured to identify lowermost mantle anisotropy, although some challenges exist. Here, we use global wavefield simulations to evaluate commonly used approaches to inferring a lowermost mantle contribution to ScS splitting. We show that due to effects of the CMB reflection, only the epicentral distance range between 60° and 70° is appropriate for ScS splitting measurements. For this distance range, splitting is diagnostic of deep mantle anisotropy if no upper mantle anisotropy is present; however, if ScS is also split due to upper mantle anisotropy, the reliable diagnosis of deep mantle anisotropy is challenging. Moreover, even in the case of a homogeneously anisotropic deep mantle region sampled from a single azimuth by multiple ScS waves with different source polarizations (in absence of upper mantle anisotropy), different apparent fast directions are produced. We suggest that ScS splitting should only be measured at “null” stations and conduct such an analysis worldwide. Our results indicate that seismic anisotropy is globally widespread in the deep mantle.

1 Introduction

Convective flow in Earth can lead to the preferential alignment of minerals, causing waves to travel through the material with different speeds dependent on propagation and polarization directions, a property called seismic anisotropy (e.g., Silver and Chan, 1991; Long and Becker, 2010). Analogous to optical birefringence, shear waves split into a fast and a slow traveling component in seismically anisotropic materials (e.g., Silver and Chan, 1991). Seismic anisotropy has been found to be most prominent in the upper and lower layers of Earth’s mantle, while it is almost absent in the bulk of the lower mantle (e.g., Panning and Romanowicz, 2006; Chang et al., 2015). For example, anisotropy has been measured in Earth’s crust (e.g., Barruol and Kern, 1996; Haws et al., 2023), the upper mantle (e.g., Silver, 1996;

*Corresponding author: jonathan.wolf@yale.edu

32 Savage, 1999; Zhu et al., 2020), the mantle transition zone (e.g., Yuan and Beghein, 2014; Chang and Ferreira, 2019)
33 and the uppermost lower mantle (e.g., Foley and Long, 2011; Mohiuddin et al., 2015). Moreover, the lowermost 200-
34 300 km of the mantle, also called D'' , is anisotropic in many places (e.g., Kendall and Silver, 1996; Garnero and Lay,
35 1997; Nowacki et al., 2010; Reiss et al., 2019; Nowacki and Cottaar, 2021; Wolf et al., 2024; see summary by Wolf et al.,
36 2023c).

37 On average, seismic anisotropy in Earth's upper mantle is stronger than at the base of the mantle (e.g., Panning
38 and Romanowicz, 2006; French and Romanowicz, 2014). It is thus challenging to measure seismic anisotropy in the
39 lowermost mantle because the potential contribution of upper mantle anisotropy to every seismogram needs to be
40 accounted for, as the seismic waves used to infer D'' anisotropy travel through the upper as well as the deepest mantle
41 (e.g., Wolf et al., 2022b). To account for the upper mantle contribution, multiple techniques have been developed,
42 most of which rely on comparisons of the shear wave splitting contribution to multiple seismic waves. A popular
43 method to infer deep mantle anisotropy is from differential splitting of the SKS and SKKS phase (e.g., Wang and Wen,
44 2004; Niu and Perez, 2004; Long, 2009; Reiss et al., 2019; Wolf et al., 2024). SKS and SKKS have very similar raypaths
45 through the upper mantle and a much larger spatial raypath separation in the lowermost mantle. Therefore, large
46 differences in SKS and SKKS splitting for the same source-receiver pair must be due to lowermost mantle anisotropy
47 (e.g., Niu and Perez, 2004; Wang and Wen, 2004). Alternatively, the splitting of SKS and S_{diff} can be compared. If SKS is
48 not influenced by seismic anisotropy but S_{diff} clearly is, this is evidence for deep mantle anisotropy causing splitting
49 of S_{diff} (Cottaar and Romanowicz, 2013; Wolf et al., 2023b; Wolf and Long, 2023). The advantage of measurements
50 using SKS, SKKS and S_{diff} waves is that the source-side anisotropy contribution in the upper mantle is either erased
51 by the P-to-SV conversion at the core-mantle boundary (CMB; SKS and SKKS) or, under certain conditions, negligible
52 (S_{diff} ; Wolf et al., 2023b). A technique that explicitly accounts for source-side and receiver-side anisotropy is S-ScS
53 differential splitting (Wookey et al., 2005). After applying explicit ray-theoretical corrections to S and ScS for known
54 receiver-side anisotropy, source-side anisotropy can be measured from the corrected S phase. After correcting ScS
55 for the source-side contribution, the remaining anisotropy contribution to ScS must be due to D'' anisotropy (Wookey
56 et al., 2005b; Nowacki et al., 2010; Creasy et al., 2017; Pisconti et al., 2023).

57 These differential splitting techniques make a number of assumptions, typically in the context of ray theory.
58 These assumptions have been tested using global wavefield simulations. For example, the interpretation of differ-
59 ential $SV_{\text{diff}}\text{-}SH_{\text{diff}}$ travel times as being uniquely indicative of D'' anisotropy has been questioned (Komatitsch et al.,
60 2010; Borgeaud et al., 2016; Parisi et al., 2018) as isotropic models can induce $SV_{\text{diff}}\text{-}SH_{\text{diff}}$ travel time differences under
61 certain circumstances. The SKS-SKKS differential splitting technique, on the other hand, has largely been shown to
62 reliably detect anisotropy if certain caveats are considered (Tesoniero et al., 2020; Wolf et al., 2022b; see also, Lin
63 et al., 2014). Nowacki and Wookey (2016) pointed out that some of the ray-theoretical assumptions do not always hold
64 for the S-ScS differential splitting technique, especially in case of heterogeneous anisotropy. In particular the as-
65 sumption of a horizontal ScS raypath through D'' is a significant oversimplification. Additionally, Wolf et al. (2022b)
66 showed that the phase shift of the radial component of ScS due to the reflection off the mantle-core interface needs
67 to be explicitly considered to accurately measure ScS splitting. Also, Parisi et al. (2018) demonstrated that differential
68 ScS SV-SH travel times can be produced by isotropic structure at distances $> 90^\circ$. Some of these challenges could

69 successfully be resolved; for example, the horizontal raypath assumption has been avoided in recent S-ScS differ-
70 tial splitting studies (e.g., [Pisconti et al., 2023](#); [Asplet et al., 2023](#)). However, there still are many open questions, the
71 answers to which will help our ability to use ScS to measure deep mantle anisotropy.

72 In this work, we assess in detail how ScS waves can be used to measure D'' anisotropy. To do so, we address sev-
73 eral questions. First, we analyze the effects of the CMB reflection on the polarization of ScS, and how they influence
74 the measured ScS splitting parameters. Second, we use global wavefield simulations to investigate whether and how
75 apparent shear-wave splitting can be produced for isotropic input models. Here we use the term ‘shear-wave splitting
76 measurements’ to refer to the measurement of splitting parameters (delay time, fast polarization direction, splitting
77 intensity) and not simply to differential SV-SH delay times. (This distinction is important, because shear-wave split-
78 ting defined in this way includes requirements regarding the waveform’s shape.) Third, we analyze how well the
79 source-side correction of the S-ScS splitting technique works in light of the polarization effects to ScS due to its CMB
80 reflection and the slightly different raypaths of S and ScS in the source-side upper mantle. Fourth, we assess the ac-
81 curacy of explicit ScS receiver-side anisotropy corrections using a realistic forward modeling framework. Putting all
82 these insights together, we suggest a strategy for inferring deep mantle anisotropy from the shear wave splitting of
83 ScS waves. Fifth, we apply this strategy globally to analyze deep mantle anisotropy using suitable broadband seismic
84 stations. We find evidence for seismic anisotropy in regions that have been analyzed in previous studies, such as
85 beneath the northern Pacific Ocean, the Caribbean and northern Asia, but we also identify deep mantle anisotropy
86 in previously unexplored regions such as beneath southern Russia and the southwestern Pacific Ocean. Finally, we
87 discuss ways forward to improve the reliability of ScS splitting measurements and interpretations for D'' anisotropy
88 studies.

89 **2 Methods**

90 **2.1 Global wavefield simulations**

91 We use the global wavefield modeling code AxiSEM3D ([Leng et al., 2016; 2019](#)) in this work. While the code can handle
92 arbitrary three dimensional input models, it calculates synthetic seismograms very efficiently in axisymmetric input
93 models, at the same speed as the older AxiSEM code ([Nissen-Meyer et al., 2014](#)). We mostly conduct simulations using
94 axisymmetric models such as isotropic PREM ([Dziewonski and Anderson, 1981](#)), which we always use as background
95 model, following our previous work (e.g., [Wolf et al., 2022a](#)). We always consider PREM-attenuation and Earth’s
96 ellipticity in our simulations. In some simulations (see below), we replace PREM’s mantle velocity structure with the
97 tomographic model S40RTS ([Ritsema et al., 2011](#)). We carry out numerical experiments with and without seismic
98 anisotropy in the lowermost and/or upper mantle. In all simulations presented in this work, we compute synthetic
99 seismograms down to minimum periods of 5 s.

100 Our source-receiver configuration is shown in Figure 1a. We place a strike-slip earthquake at the north pole and
101 stations at epicentral distances of 60° to 100° (spaced in 1° distance increments) between longitudes 0° to 90° (spaced
102 in 10° increments). We choose event depths of either 100 m or 500 km. A strike-slip focal mechanism is selected such
103 that the initial source polarization of S and ScS is purely SH for longitudes 0° and 90° and purely SV for longitude 45°
104 (Figure 1). For each candidate event depth, we conduct three types of simulations:

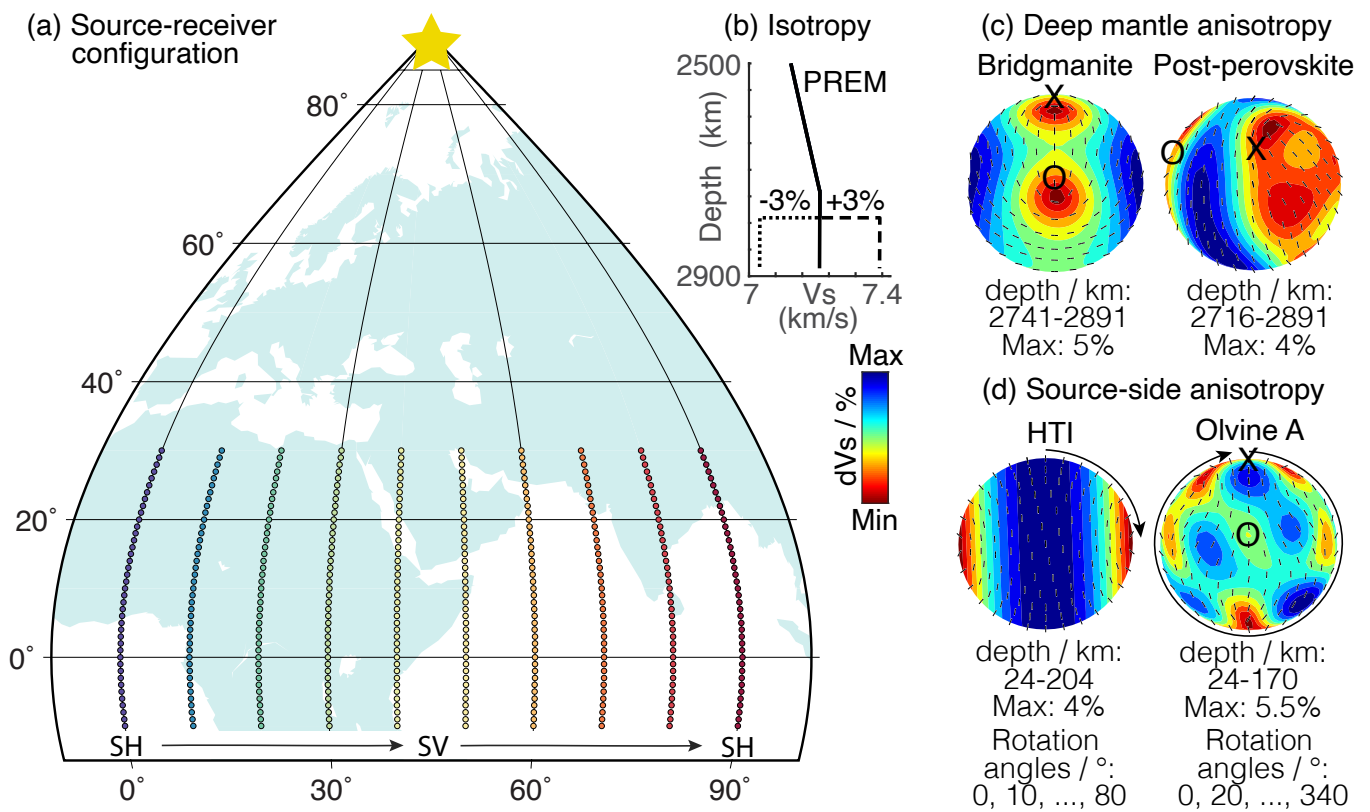


Figure 1 Source-receiver configuration and input models of synthetic simulations. (a) Source and receivers: The strike-slip event (see text) is shown as a yellow star; stations are represented as dots, colored by longitude (which corresponds to the initial polarization of the arriving wave). (b) Lowermost mantle velocity as a function of depth for the PREM model, PREM with 3% reduced (dotted line), and 3% increased velocities (dashed line). All these scenarios are used in our synthetic modeling. (c) Upper hemisphere representations of the elastic tensors (bridgmanite, post-perovskite) used in simulations in which we incorporate deep mantle anisotropy (at the depths shown below each elastic tensor plot). The elastic tensors were taken from the elastic tensor library of [Creasy et al. \(2020\)](#). The color scale shows the percentage of S-wave anisotropy as a function of direction. The maximum percentage is shown at the bottom and depends on the elastic tensor. The small black sticks indicate the fast polarization direction of the S wave for the corresponding propagation direction. The black 'O' represents the shear-plane normal and 'X' the shear direction. The lowermost mantle elastic tensors are oriented such that robust shear-wave splitting measurements can be obtained. (d) Similar to panel (c), for upper mantle source-side anisotropy. The elastic tensor rotation performed in this work is indicated by arrows. The HTI elastic tensor was calculated using MSAT ([Walker and Wookey, 2012](#)) and the olivine type-A elastic tensor was taken from [Karato \(2008\)](#).

1. Isotropic simulations:

- (a) using isotropic PREM (Figure 1b) as input model;
- (b) incorporating modified velocities in the lowermost 150 km of the mantle, replacing those of PREM (Figure 1b);
- (c) incorporating a 3D tomography model (S40RTS) in the mantle, replacing PREM velocities.

2. Anisotropic simulations with lowermost mantle anisotropy:

- (a) incorporating bridgmanite (Br) anisotropy in the lowermost 150 km of the mantle;
- (b) incorporating post-perovskite (Ppv) anisotropy in the lowermost 175 km of the mantle.

These elastic tensors were taken from [Creasy et al. \(2020\)](#) and are displayed as upper hemisphere representations in Figure 1c. The use of these elastic tensors leads to slightly different lowermost mantle velocities than

PREM. The main goal of these simulations is to evaluate the influence of realistic lowermost mantle anisotropy on ScS seismic waves; the isotropic effects are analyzed in the previous set of simulations.

3. Anisotropic simulations with upper mantle anisotropy:

- (a) using horizontal transverse isotropy (HTI) in the upper mantle (Figure 1d). The HTI elastic tensor is calculated using MSAT (Walker and Wookey, 2012) and incorporated at the depth range of 24 km to 204 km.
- (b) using olivine (A-type fabric) anisotropy in the upper mantle (Figure 1d). The elastic tensor is from Karato (2008) and the anisotropy is incorporated at the depth range of 24 km to 170 km.

In both cases, the anisotropy in the upper mantle leads to a maximum delay time of ~ 1.5 s. In order to sample anisotropy from different directions, the elastic tensors are rotated around the vertical axis (with respect to their representations in Figure 1d) for different simulations. Due to its symmetry, the HTI elastic tensor is only rotated by angles of 0° to 80° (in 10° increments), while the olivine elastic tensor is rotated between 0° to 340° (in 20° increments).

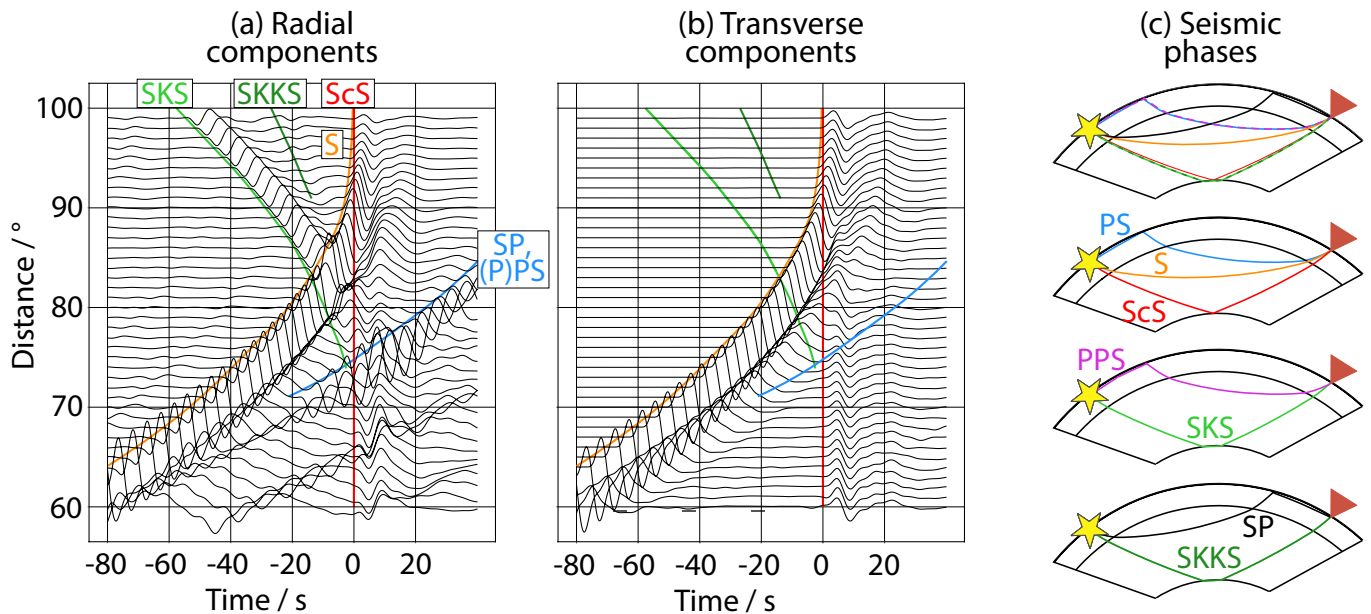


Figure 2 Synthetic waveforms as a function of distance for stations placed along longitude 70° (Figure 1), with sketch of relevant seismic phases. (a) Radial component displacement waveforms, plotted at every 1° distance increment. Incoming high-amplitude seismic phases are marked with colored lines. (b) Same as panel (a) for the transverse component. (c) Schematic diagrams of raypaths through Earth for the seismic phases marked in panels (a) and (b). The source is shown as a yellow star and the station, at an epicentral distance of 70° , as a red triangle.

Synthetic radial and transverse seismograms as a function of distance (for PREM as input model), aligned on the predicted ScS arrival, are shown in Figure 2a,b. At an epicentral distance of around 75° , interference from the PS and PPS phases, which arrive very close together in time at these distances, can be observed. Additionally, some SP energy (which arrives contemporaneously to PS for a 0 km deep source) likely arrives on the radial component. While PS interference can be observed in the record section shown in Figure 2, the phase is not observable at this distance range for events with focal depths deeper than 200 km, although some PPS energy may still be relevant. For distances $> 80^\circ$, ScS starts to merge with S. For distances $< 70^\circ$ and $> 63^\circ$, SKS and ScS arrive almost contemporaneously, although it is unclear whether SKS has a sufficiently large amplitude to noticeably influence ScS. (A partial answer to

135 this question will be discussed in Section 4.) The raypaths of the seismic phases that may potentially interfere with
 136 ScS are shown in a cross-section in Figure 2c.

137 **2.2 Shear wave splitting measurements**

138 Shear wave splitting, which is analogous to optical birefringence, is a consequence of seismic anisotropy. A shear
 139 wave that travels through an anisotropic medium splits into a fast and a slow component. The time lag between
 140 these components is called δt and the polarization direction of the fast traveling wave is usually referred to as ϕ when
 141 measured clockwise from the north, or ϕ' (Nowacki et al., 2010) when measured with respect the incoming wave's
 142 backazimuth. Another quantity that is frequently used is the splitting intensity (Chevrot, 2000), SI , which yields a
 143 scalar value indicating the splitting strength on an individual seismogram. The splitting intensity is defined as:

$$144 \quad SI = -2 \frac{Pol_{90}(t) Pol'_0(t)}{|Pol'_0(t)|^2} \approx \delta t \sin(-2\phi'), \quad (1)$$

145 with $Pol'_0(t)$ denoting the time derivative of the component in the direction of initial polarization, whereas $Pol_{90}(t)$
 146 is the horizontal seismogram component oriented 90° away from the incoming wave's primary polarization.

147 We determine the splitting parameters (ϕ , δt) using a modified version of the SplitRacer software (Reiss and Rump-
 148 ker, 2017), which is the same version previously used by Wolf et al. (2022b). This version estimates the initial polar-
 149 ization of the incoming wave, through particle motion analysis, as ScS waves are not typically initially SV-polarized.
 150 SplitRacer calculates the splitting parameters (ϕ , δt) using the transverse energy minimization technique (Silver and
 151 Chan, 1991), incorporating a corrected calculation of the 95% confidence intervals (Walsh et al., 2013). Whenever
 152 we apply source-side anisotropy corrections for the S-ScS differential splitting technique, we measure source-side
 153 anisotropy splitting parameters with SplitRacer. Then, we use a code to correct the ScS phase for these source-side
 154 splitting parameters, following the algorithm described in Wolf et al. (2022b), which is based on work from Wookey
 155 et al. (2005). In this algorithm, we also calculate splitting parameters using the transverse energy minimization tech-
 156 nique, building upon an implementation from Creasy et al. (2017). For all these measurements, we consider (ϕ , δt)
 157 measurements well-constrained if the 95% confidence intervals are smaller than $\pm 25^\circ$ for ϕ , ± 0.8 s for δt and ± 0.5 for
 158 SI . Before measuring splitting parameters, we filter our seismograms retaining periods between 5 s and 15 s (unless
 159 specified differently). Polarizations are determined from the seismograms at longer periods (8-25 s) from the long
 160 axis of the particle motion ellipse.

161 **3 SV reflection coefficients of ScS at the CMB**

162 In order to understand the potential effects of the CMB reflection on ScS phases, we solve the equations of Chapman
 163 (2004) to calculate SV reflection coefficients of ScS at the CMB for PREM velocity structure in the whole mantle, as well
 164 as for 3% reduced and increased velocities with respect to PREM in the lowermost 150 km of the mantle (Figure 3).
 165 Such velocity variations are realistic for Earth's faster and slower lowermost mantle regions (e.g., Ritsema et al., 2011).
 166 We also explore variations of the reflection coefficients as a function of source depth and do not find any substantial
 167 differences compared to the 0 km case shown in Figure 3. We do not compute SH reflection coefficients as the shear
 168 wave velocity in the outer core is zero and SH does not couple with P; therefore, all SH energy will be reflected without

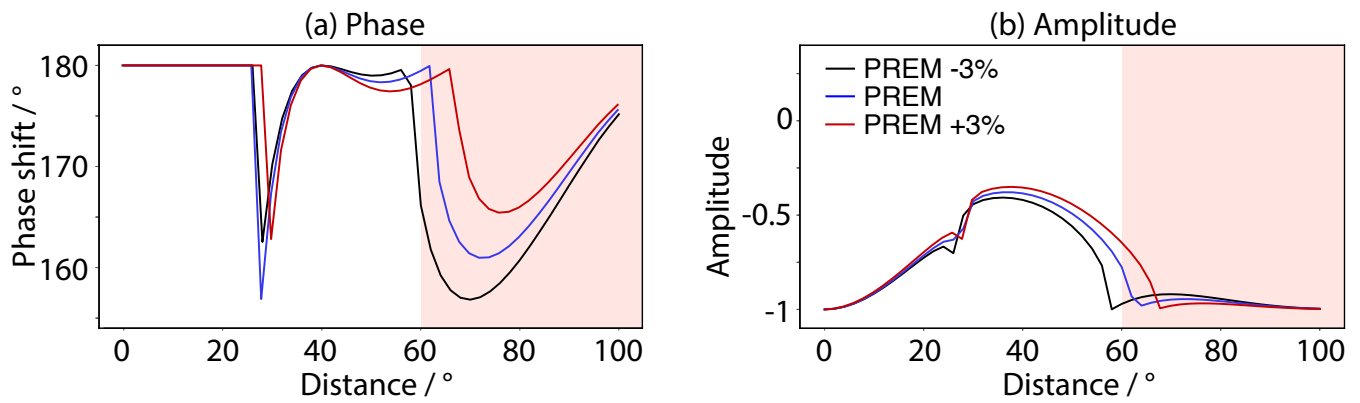


Figure 3 Influence of the CMB reflection on the SV portion of the ScS phase. We calculate reflection coefficients for PREM (blue line), PREM -3% (black line), and PREM +3% (red line) shear velocities in the lowermost 150 km of the mantle (Figure 1b). The source depth for this calculation is 0 km, but we note that no significant variation can be observed as a function of source depth. Red shading marks epicentral distances $> 60^\circ$, which are typically used for measurements of shear-wave splitting due to lowermost mantle anisotropy. (a) Phase shift of the radial component of the ScS as a function of epicentral distance. (b) Amplitudes (real part of the reflection coefficient) as a function of epicentral distance.

169 a phase or amplitude change. Several observations can be made from Figure 3:

- 170 • For distances $< \sim 60^\circ$, SV amplitudes are strongly reduced after the reflection. For example, at an epicentral
171 distance of $\sim 30^\circ$ SV loses $\sim 70\%$ of its amplitude. This pattern depends on the lowermost mantle velocity and
172 is therefore only possible to account for exactly if the velocity structure at the reflection point is well known.
173 While the SV amplitude effects are complicated, for most distances $< \sim 60^\circ$ the SV phase shift is simple and
174 close to 180° (Figure 3).
- 175 • For epicentral distances $< 10^\circ$, SV will simply undergo a sign-flip with amplitudes almost unaffected by the
176 reflection.
- 177 • For epicentral distances $> \sim 60^\circ$, SV amplitudes are largely unchanged by the reflection and the SV phase shift
178 is between 160° and 180° , depending on distance and deep mantle velocity structure (Figure 3). Because of
179 this, [Wolf et al. \(2022b\)](#) suggested that the description of SV behavior at distances $> \sim 60^\circ$ as a simple sign-flip
180 is accurate enough for the purpose of ScS splitting measurements.

181 Our analysis of distance-dependent SV reflection coefficients for ScS shows that it is difficult to infer the presence
182 of deep mantle anisotropy for ScS waves at epicentral distances $< \sim 60^\circ$. For these epicentral distances, relative SV-SH
183 amplitudes will be strongly influenced by the deep mantle velocity structure of the region under study, which needs to
184 be precisely accounted for. However, this appears challenging, as the deep mantle velocity structure in any particular
185 deep mantle region is often poorly known. We therefore focus our following analysis on epicentral distances $> 60^\circ$,
186 which is the most frequently used distance range. For example, the S-ScS differential splitting technique has been
187 suggested to be applicable at a distance range between 60° and 85° ([Wookey et al., 2005](#)). There are also multiple
188 previous studies that have analyzed the behavior of S and ScS waves at distances $> \sim 85^\circ$ (e.g., [Kendall and Silver,](#)
189 [1996](#); [Pulliam and Sen, 1998](#); [Fouch et al., 2001](#)) to infer deep mantle anisotropy.

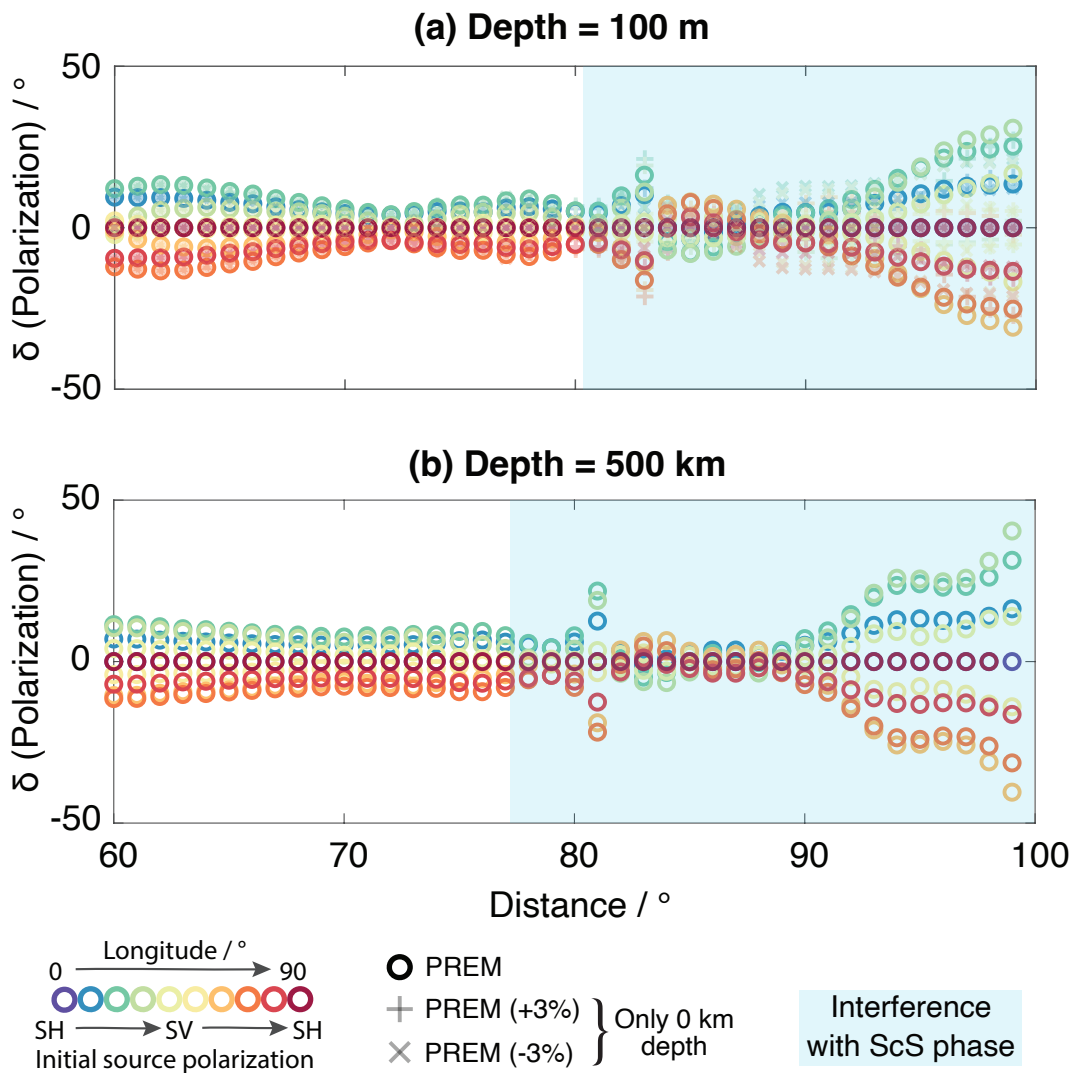


Figure 4 Measured S polarizations relative to the initial source polarization as a function of epicentral distance, for different deep mantle velocity profiles (legend), initial source polarizations (legend), and source depths. Potential interference with ScS is indicated by blue shading. Measurements are conducted for source depths of (a) 100 m and (b) 500 km.

4 S and ScS polarizations in isotropic input models

Next, we analyze S and ScS polarizations at epicentral distances between 60° and 100° using global wavefield simulations. We conduct synthetic simulations for PREM velocity structure in the whole mantle as well as for 3% increased and reduced velocities above the CMB (Figure 1a). In Figure 4, we show measured S polarizations for different initial source polarizations of the wave and source depths of 100 m and 500 km. The results are only weakly influenced by the lowermost mantle velocity, but do depend on source depth for distances $> 90^{\circ}$. Figure 2 shows that the S wave polarizations are relatively unaffected by interference from other seismic phases at distances $< 80^{\circ}$, but start to be influenced by ScS at greater distances. Accordingly, measured S polarizations agree very well with the initial source polarizations for distances $< 80^{\circ}$ (Figure 4). For larger distances, S polarizations are influenced by ScS but still largely agree with the initial source polarization (Figure 4).

For ScS, the pattern of measured polarizations as a function of distance is more complicated (Figure 3). At epicentral distances between 60° and 70° , ScS initial polarizations are approximately opposite the S wave polarization as controlled by the source (Figure 5) due to the approximate SV sign-flip (Figure 3). However, because the sign-flip

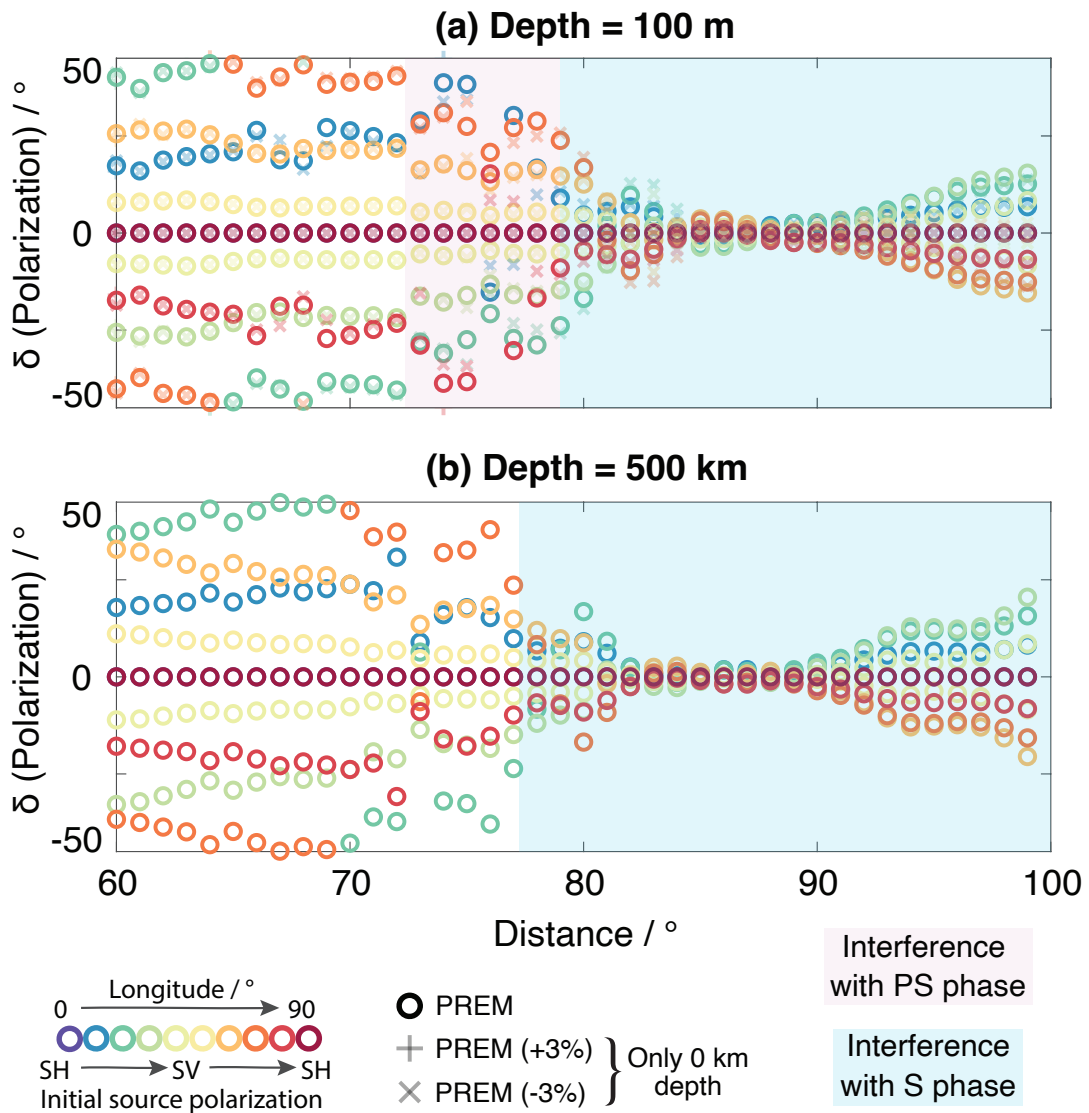


Figure 5 Same as Figure 4 for ScS. Potential PS interference is indicated by pink shading and potential S interference by blue shading.

203 of SV is not exact (Figure 3), and because of the potential interference with SKS in some of the epicentral distance
 204 range (Figure 2), this pattern is by no means perfect. These two effects are hard to distinguish; however, analyzing
 205 them in isolation is not required to understand the conditions under which ScS can be used for analyses of lowermost
 206 mantle anisotropy, which is the main goal of this study. For distances between 73° and 79° , interference with PS can
 207 lead to estimated polarizations close to SV (Figure 5a). For deep sources (Figure 5b), no PS energy arrives; however,
 208 PPS and SP may still influence ScS waveforms around this distance range. Exceptions are observed at the stations
 209 at azimuths for which the initial polarization is purely SH, as the (P)PS amplitude is zero for them (Figure 5). For
 210 distances $> 80^{\circ}$, S and ScS merge, with S dominating, leading to polarizations that are close to the S initial source
 211 polarization (Figure 5). These overall patterns hold for all the different lowermost mantle velocities that we tested
 212 (Figure 5).

213 Considering these results, it appears challenging to measure deep mantle anisotropy reliably from ScS for dis-
 214 tances at which the PPS or PS phase potentially interferes with ScS. This corresponds to a distance range between
 215 73° and 79° for shallow events (e.g., Figure 5) and to distances down as close as 70° for an event depth of 150 km.

216 For events deeper than ~ 200 km no PS phase arrives at these distances, but PPS may have an influence on seismic
 217 waveforms down to 70° epicentral distance. Similarly, if shear wave splitting is measured from S/ScS for distances
 218 $\sim > 80^\circ$, it should be considered that the S initial polarization likely dominates, but ScS influences the waveforms
 219 and horizontal component amplitude ratios.

220 5 Apparent shear-wave splitting in isotropic input models

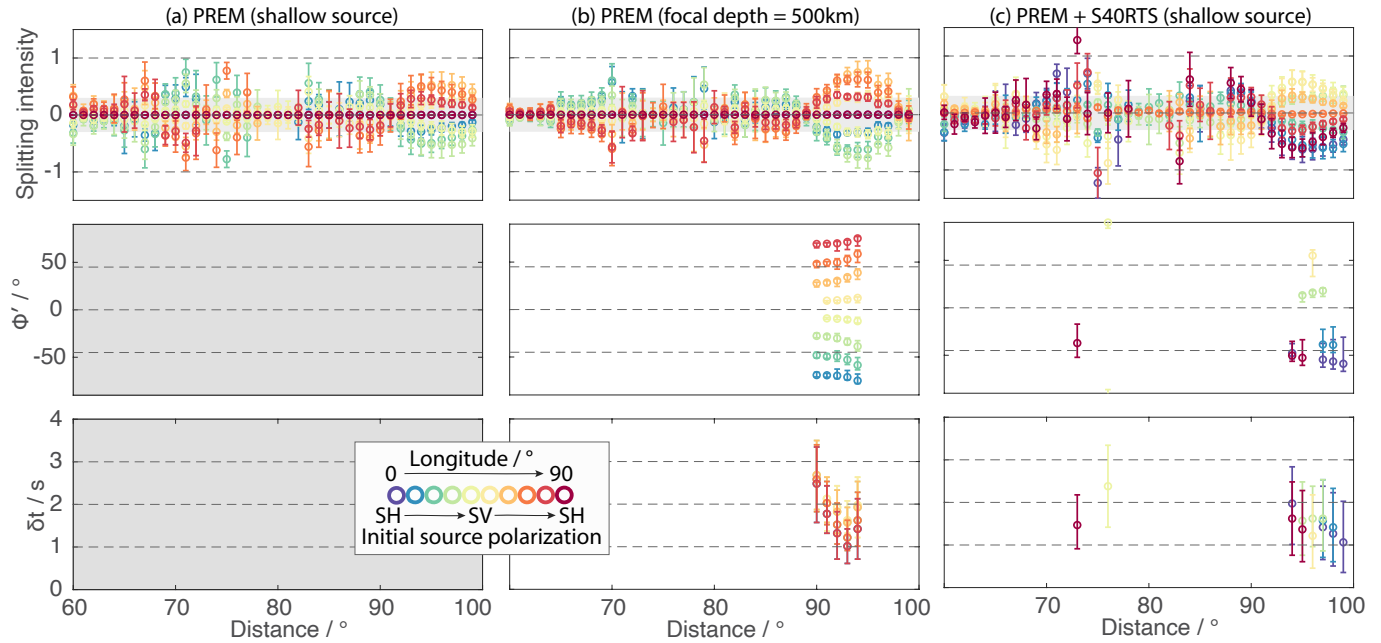


Figure 6 Shear wave splitting parameters SI (top), ϕ' (middle), δt (bottom) as a function of distance, dependent on initial source polarization (legend), for isotropic input models. Error bars indicate 95 % confidence intervals of the measurements (see Section 2.2). Only well-constrained splitting measurements are shown (see text). (a) For PREM input model and a focal depth of 100 m. (b) For PREM input model and a focal depth of 500 km. (c) For PREM input model, for which the mantle was replaced with the tomographic model S40RTS, and a focal depth of 100 m. Apparent shear-wave splitting can be produced at distances $> 90^\circ$, but also sometimes at smaller distances.

221 We have shown how the CMB reflection and phase interferences can influence the polarization of ScS. However,
 222 it remains unclear whether such effects can result in apparent shear wave splitting. To test this, we conduct synthetic
 223 simulations in isotropic input models as introduced in Section 2.1.

224 For PREM synthetics, calculated for a focal depth of 100 m, non-null splitting intensities can be reproduced, al-
 225 though we do not measure well-constrained splitting parameters (ϕ , δt) (Figure 6a). If the source is placed in a depth
 226 of 500 km, however, apparently well-constrained (ϕ , δt) values can be measured at distances between 90° and 94°
 227 (Figure 6b). Some of these measurements may be identified as null splitting, but not all of them. For PREM+S40RTS,
 228 on the other hand, apparently well-constrained (ϕ , δt) values are mainly obtained for distances $> 94^\circ$ (although there
 229 is also some apparent splitting at smaller distances). The reason for the apparent splitting is phase interference; for
 230 example, the interaction between S and ScS (Figure 2), which arrive at approximately the same time for distances
 231 $> 90^\circ$. The transverse components of S and ScS are generally very similar at these distances, as the transverse ScS
 232 component is largely unaffected by the reflection. However, the radial ScS component will be approximately sign-
 233 flipped compared to S (Figure 3) and potentially have a slightly different amplitude; the details of the phase's behavior
 234 depend on lowermost mantle velocity structure and the event depth (Figure 3). If these waveform distortions affect

235 transverse and radial components in a way that the energy on the Pol component has the shape of the time derivative
 236 of the Pol_{90} component, apparent splitting results.

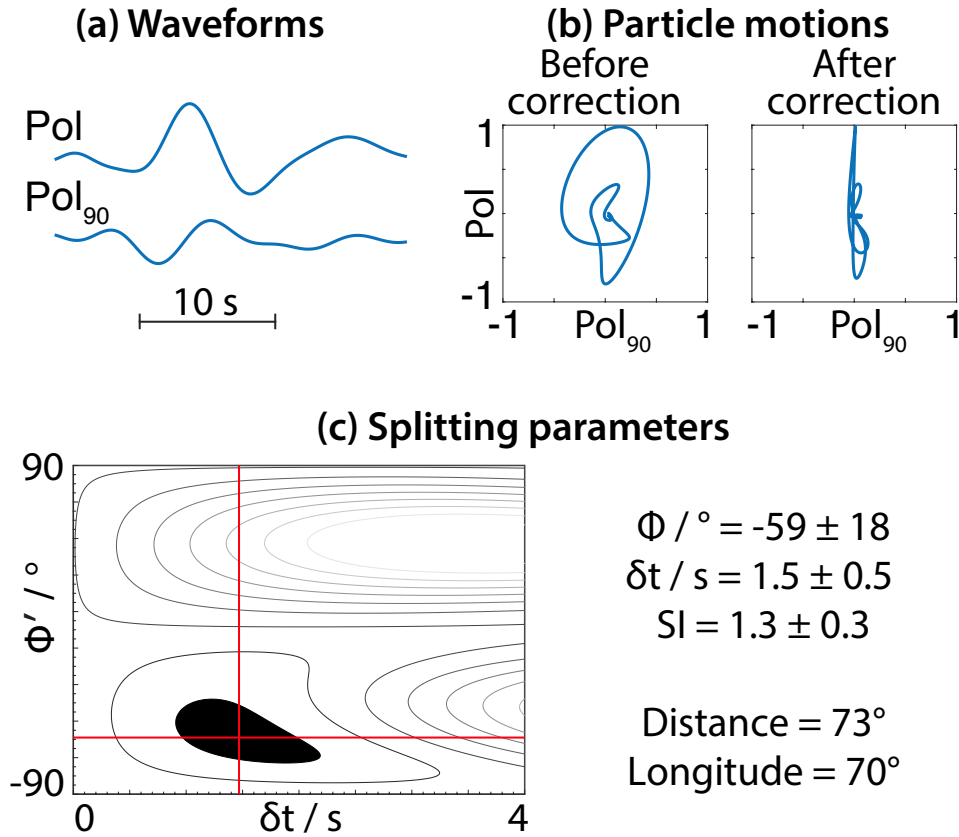


Figure 7 Example apparent shear wave splitting for the (isotropic) PREM+S40RTS input model and a source depth of 0 km. (a) Pol and Pol_{90} waveforms for the combined ScS phase. (b) Particle motions before (left) and after (right) correction for the best-fitting splitting parameters. (c) Best-fitting splitting parameters in the ϕ' - δt plane. The 95% confidence interval is shown in black.

237 We show an example of apparent shear-wave splitting from simulations using isotropic PREM+S40RTS with a
 238 source at 100 m depth in Figure 7. The Pol_{90} component has approximately the shape of the Pol_0 component time
 239 derivative (Figure 7a) and the particle motion looks elliptical (Figure 7b), mimicking shear wave splitting due to seis-
 240 mic anisotropy. Accordingly, the apparent estimated splitting parameters are well-constrained (Figure 7c).

241 Our results so far indicate that measurements of shear-wave splitting for epicentral distances $< 60^\circ$ need to care-
 242 fully consider the SV reflection coefficient at the CMB for ScS, which will depend on the deep mantle velocity structure
 243 of the region under study. Additionally, distances between 70° and 80° cannot be used for ScS splitting measurements
 244 if (P)PS or SP may be interfering. For distances $> 80^\circ$, S and ScS merge (Figure 2), making it challenging to distin-
 245 guish between these phases in seismograms. Apparent splitting of the combined S/ScS phase can be produced in
 246 isotropic structure (Figures 6 and 7). Therefore, the most promising distance range to measure ScS splitting due to
 247 deep mantle anisotropy is between 60° and 70° .

248 6 Shear wave splitting in models that incorporate deep mantle anisotropy

249 We next test the effects of deep mantle anisotropy on measured ScS splitting in absence of upper mantle anisotropy,
 250 incorporating Br (Figure 8a) and Ppv (Figure 8b) anisotropy in the lowermost mantle, replacing PREM velocity struc-
 251 ture (see Section 2.1). In Figure 8 we show measured shear wave splitting parameters (SI ; ϕ' , δt) from ScS as a func-

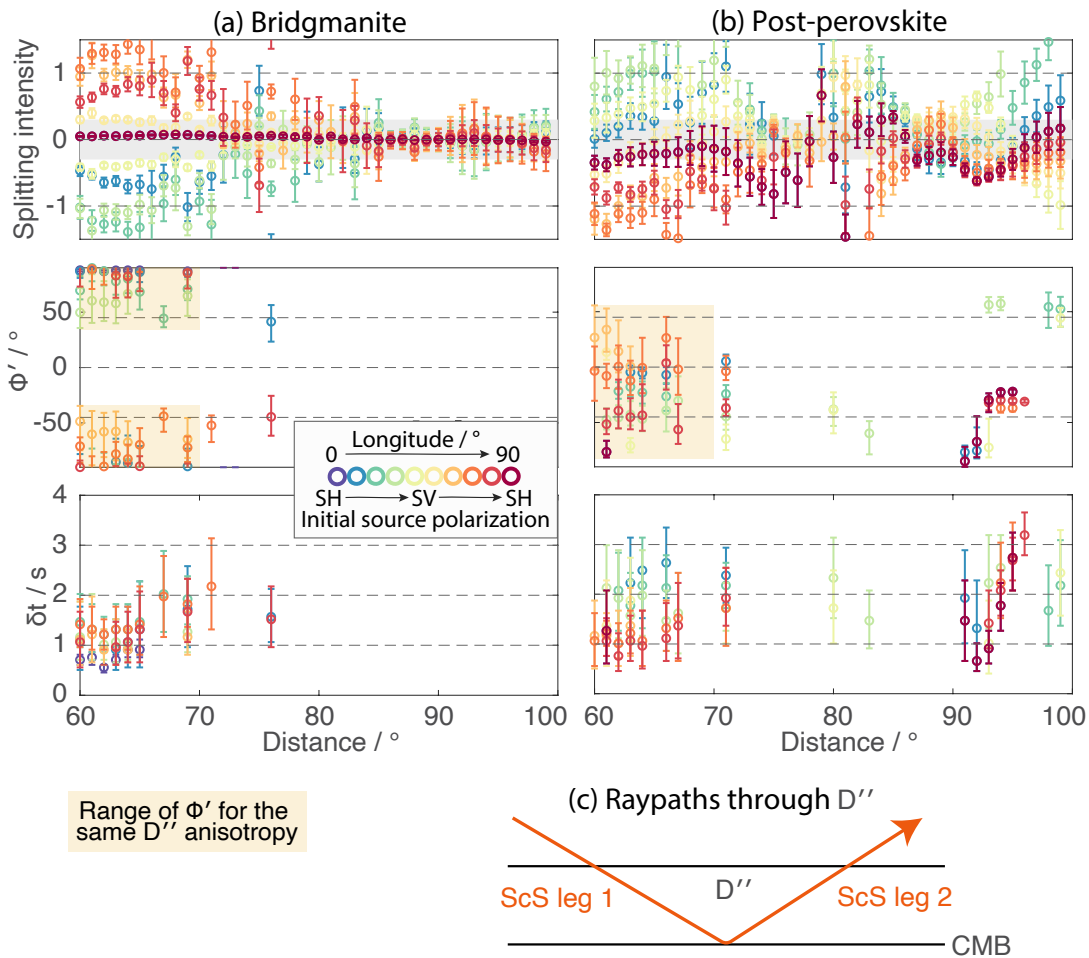


Figure 8 Shear wave splitting parameters for input models that include global layers of lowermost mantle anisotropy and no seismic anisotropy in the upper mantle. (a) Results for a 150 km thick layer of Br anisotropy at the base of the mantle and PREM-velocities otherwise. Same plotting conventions as in Figure 6a. The range of ϕ' values for the same deep mantle anisotropy, sampled from the same direction, but for different ScS initial source polarizations (see legend), is indicated by orange shading. (b) Results for a 175 km thick layer of Ppv anisotropy at the base of the mantle and PREM-velocities otherwise. Same plotting conventions as in panel (a). (c) Schematic illustration of the two ScS raypath legs through D'' . Because the measured shear wave splitting is a combination of the sampled seismic anisotropy on both legs of the raypath and the initial source polarization, a range of ϕ' values is obtained when sampling the same seismic anisotropy from the same direction for differently polarized ScS waves.

252 tion of epicentral distance and initial source polarization. Due to the aforementioned challenges at many epicentral
 253 distances, we focus on shear wave splitting measured at distances between 60° and 70° . In this distance range, we
 254 measure many well-constrained $(\phi', \delta t)$ values for our anisotropic input models (Figure 8). The seismic anisotropy
 255 in the input model is incorporated such that it is sampled from the same direction independent of azimuth. How-
 256 ever, we can observe a large spread of measured ϕ' values for both elastic tensors we tested. The reason for this is
 257 that the measured splitting is a combination of the splitting accumulated on both legs of the ScS raypath through
 258 D'' (Figure 8c). The initial polarization of ScS depends on its azimuth in our simulations, and this initial polarization
 259 affects how the wave is split on both legs of the raypath. This situation is analogous to splitting from multiple layers
 260 of anisotropy in the upper mantle, which produces apparent splitting that depends on azimuth (Silver and Savage,
 261 1994; Silver and Long, 2011). Therefore, it is logical that measured fast polarizations are not the same, even though
 262 the same deep mantle anisotropy is sampled. As a consequence, if ScS splitting due to D'' anisotropy is measured
 263 from a certain sampling direction for any given lowermost mantle region, ScS splitting parameters $(\phi, \delta t)$ cannot be

264 expected to be the same for different events, unless the events all have similar initial polarizations. Therefore, the
 265 mean splitting measurement as often determined in ScS splitting studies (e.g., Nowacki et al., 2010; Wolf et al., 2019;
 266 Pisconti et al., 2023) does not have a clear meaning for the interpretation of mantle flow directions, since the same
 267 measurement can be obtained for a variety of anisotropy scenarios and initial polarizations of the wave.

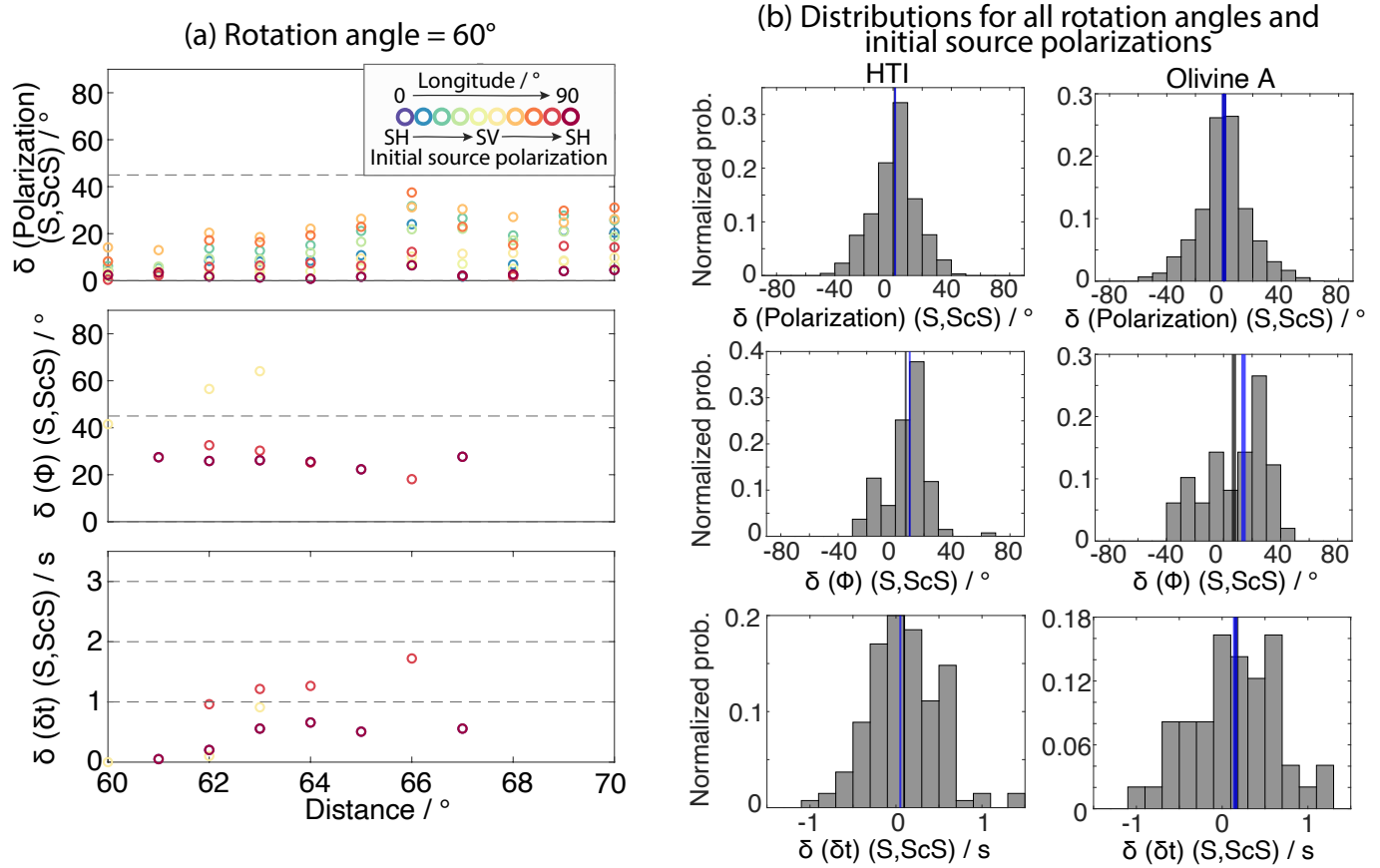


Figure 9 Differences between estimated ScS polarizations, measured fast polarization directions ϕ , and delay times δt , compared to the values that would be expected after S analysis if the radial ScS component was a perfectly sign-flipped version of the S radial component. Values are measured from synthetic waveforms generated for a model that includes source-side anisotropy only and PREM velocity structure elsewhere. Only well-constrained splitting results are shown (as defined in Section 5). (a) Example for the olivine elastic tensor shown in Figure 1c with a horizontal rotation angle of 60° (Section 2), and for different initial source polarizations (legend). Top: Absolute differences in predicted and measured ScS polarizations $\delta(\text{Polarization})$. Middle: Absolute differences in predicted and measured ScS fast polarization directions $\delta(\phi)$. Bottom: Absolute differences in predicted and measured ScS delay times $\delta(\delta t)$. (b) Histograms showing the distributions of $\delta(\text{Polarization})$ (top), $\delta(\phi)$ (middle) and $\delta(\delta t)$ (bottom) for HTI (left) and olivine (right) anisotropy (Figure 1c) for all initial polarizations and elastic tensor rotation angles (Section 2.1). Distribution means are shown as solid black lines and medians as solid blue lines.

268 7 Correction of ScS for source-side anisotropy contribution inferred from S

269 The S-ScS differential splitting technique isolates the lowermost mantle anisotropy contribution to ScS by correcting
 270 the ScS waveform for the influence of receiver-side and source-side anisotropy in the upper mantle (Wookey et al.,
 271 2005). The source-side anisotropy contribution is inferred from the S waveform, which has been first corrected for the
 272 influence of receiver-side anisotropy. The assumptions made in this process are that S and ScS raypaths through the
 273 upper mantle are sufficiently similar that both phases experience the same splitting due to upper mantle anisotropy,
 274 and that their initial source polarizations are also similar. In the most extreme case, for a source-receiver distance
 275 of 60° and a surface event, S and ScS raypaths are up to 250 km apart at the bottom of the transition zone, so that the

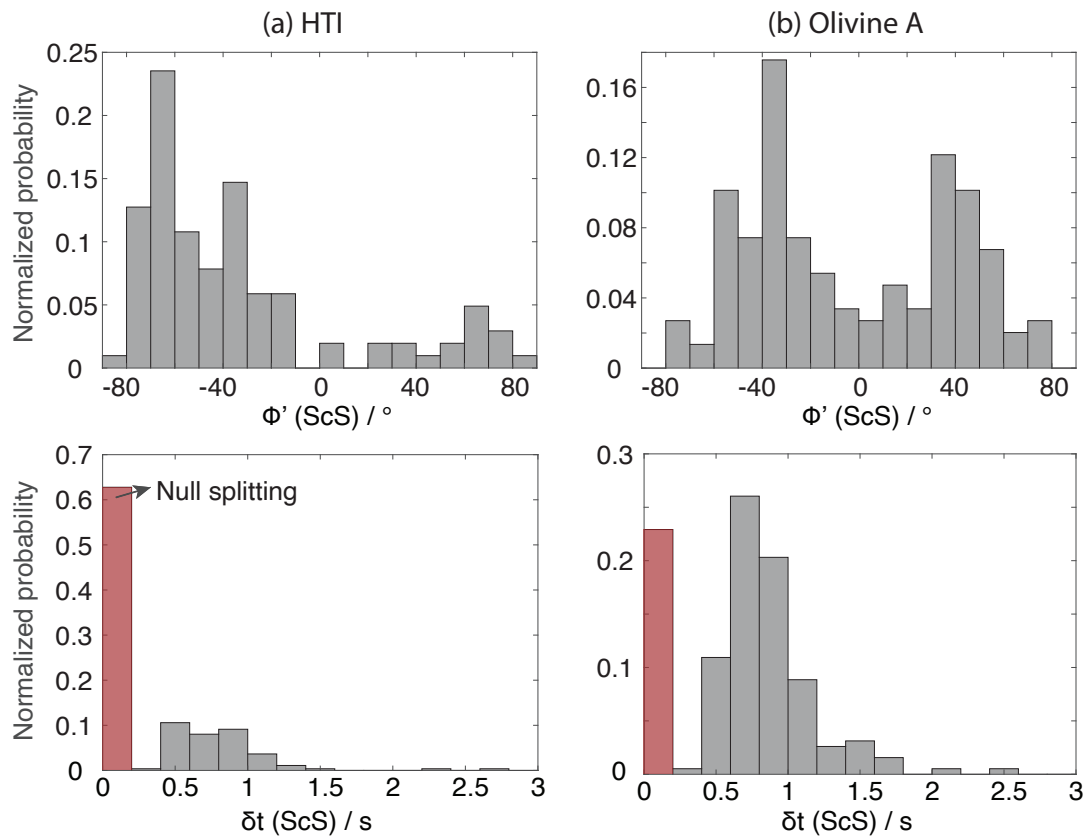


Figure 10 Distributions of measured ϕ' and δt for all initial polarizations and elastic tensor rotation angles after correcting for source-side anisotropy measured from S, only showing well-constrained results (as defined in Section 5). (a) Results for a model including HTI source-side anisotropy and PREM-velocities elsewhere. Top: ϕ' histograms; bottom: δt histograms. ϕ' values are only plotted for non-null measurements. Measurements are defined as null if the 95% confidence interval of δt overlaps with the interval $[0\text{ s}, 0.3\text{ s}]$. Null measurements are indicated in orange color. (b) Same as panel (a) for olivine A source-side anisotropy.

276 assumption that S and ScS raypaths are sufficiently close together may only be valid in cases of relatively generally
 277 homogeneous upper mantle anisotropy. To account for the CMB reflection, Wolf et al. (2022b) suggested approxi-
 278 mating the phase shift of ScS_{SV} as a simple sign-flip of the radial component. More accurate corrections would be
 279 challenging, given that the precise phase shift depends on the deep mantle velocity structure near the ScS reflection
 280 point (Figure 3). Additionally, our results for a distance range close to 60° , at which the PREM-predicted phase shift
 281 corresponds to a precise sign-flip (Figure 3), do not indicate that ScS splitting measurements could be substantially
 282 improved by implementing the PREM-predicted phase shift. Using this assumption, Wolf et al. (2022b) showed that
 283 approximate source-side splitting parameters for ScS can indeed be inferred from S. These splitting parameters can
 284 then be used to correct ScS waveforms after a correction for receiver side anisotropy has been applied (Wookey et al.,
 285 2005).

286 Measurements of the polarization of the S phase can be used to predict ScS polarization in the epicentral distance
 287 interval between 60° and 70° . Since the backazimuth is always zero for our source-receiver configuration (Figure 1a)
 288 and the radial ScS component is approximately a sign-flipped version of the S radial component (Figure 2), the sum
 289 of the S and the ScS polarizations must be approximately zero.

290 Figure 9 explores how accurately, under the assumptions described above, ScS splitting due to source-side anisotropy
 291 can be predicted from the splitting of the corresponding S phase. We do not incorporate any receiver-side or deep

292 mantle anisotropy in these simulations. We measure S and ScS polarizations and splitting parameters (ϕ , δt). Then,
293 we determine the difference between the ScS splitting parameters and those predicted from the S phase. Figure 9a
294 shows an example for olivine anisotropy in the source-side upper mantle, with the elastic tensor rotated by 60° around
295 the vertical axis (Section 2.1). The measured polarizations and fast polarization directions of ScS are different than
296 those predicted from S by up to $\sim 35^\circ$ and δt differs by up to 2 s. Summary histograms for all the results obtained using
297 a range of different rotation angles for the anisotropy geometry (Section 2.1) are shown in Figure 9b. These results
298 indicate that substantial differences between predicted source-side anisotropy associated splitting parameters from
299 S and measured splitting parameters for ScS are common. Also, the assumption of a radial component sign-flip of
300 ScS caused by the reflection is imperfect, sometimes leading to polarization differences of up to 50° .

301 Next, we systematically apply the source-side anisotropy splitting parameters, as inferred from S, to the ScS phase
302 and then measure ScS splitting. If the source-side anisotropy correction was accurate, we would expect to measure
303 null residual splitting from ScS as we did not incorporate deep mantle anisotropy in our simulations. (Recall that
304 these simulations only include upper mantle anisotropy near the source.) We define null measurements here as
305 splitting measurements which have δt -values smaller than 0.3 s, or a 95% confidence interval that overlaps with values
306 < 0.3 s. This definition leads to few well-constrained (ϕ , δt)-measurements with $\delta t < 0.5$ s in Figure 10. We find that
307 for the HTI elastic tensor, only $\sim 63\%$ of the measured ScS splitting parameters are null after applying the source-side
308 correction (Figure 10a). For olivine, this value is only $\sim 23\%$, meaning that in $\sim 77\%$ of the cases apparent D'' splitting
309 is introduced by applying the the source-side correction (Figure 10b).

310 The reason that the source-side anisotropy correction is not generally accurate is that the the source-side contri-
311 bution for ScS cannot accurately be inferred from S. In Figure 11 we show retrieved δt values for well-constrained
312 ScS splitting measurements after accounting for source-side anisotropy inferred from S. If ScS source-side splitting
313 parameters are used to correct ScS, in 98 % of the cases no apparent D'' splitting is introduced (Figure 11a), showing
314 that our correction procedure works well if splitting is perfectly known. We can use these insights to suggest three
315 different strategies for accounting for source-side anisotropy. First, we can restrict measurements of ScS splitting to
316 cases for which S source-side splitting is null (Figure 11b). Second, we can minimize the influence of source-side up-
317 per mantle anisotropy by only measuring ScS splitting from deep seismic events. However, the presence of seismic
318 anisotropy has been suggested in the uppermost lower mantle, particularly in subduction zones has been suggested
319 by several studies (e.g., [Foley and Long, 2011](#); [Lynner and Long, 2015](#); [Mohiuddin et al., 2015](#)). Therefore, such an
320 approach would not necessarily (always) be reliable. Third, we can apply a source-side anisotropy correction if we
321 measure a ScS polarization that is within 10° of the expected initial polarization for a sign-flip of the ScS radial com-
322 ponent Figure 11c). In 90 % of these cases, null D'' splitting is correctly predicted from ScS if measured S source-side
323 splitting is null (Figure 11b), suggesting that these strategies allow for the accurate consideration of source-side split-
324 ting in certain cases. In contrast, explicit source-side anisotropy corrections are inaccurate when these conditions
325 are not met, even when ensuring that the ScS polarization is as expected from S (Figure 11c).

326 **8 Correction of ScS for receiver-side anisotropy contribution inferred from SKS**

327 As discussed in Section 7, we now better understand the strengths and weaknesses of the source-side correction for

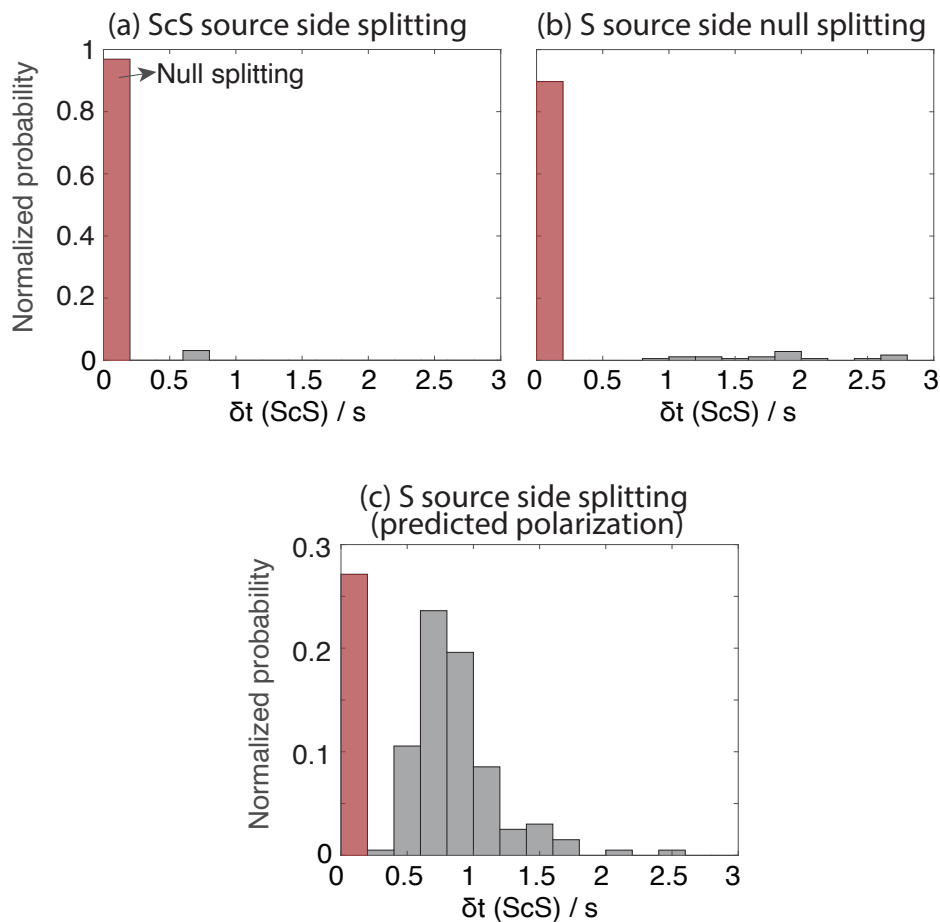


Figure 11 Retrieved δt values for well-constrained ScS splitting measurements after accounting for olivine source-side anisotropy, for the same set of simulations used in Figure 10. Only well-constrained splitting results are shown (as defined in Section 5). (a) Histograms of results obtained after correcting ScS waveforms for source-side anisotropy measured from the same ScS waveform. Plotting conventions are the same as in the bottom panel of Figure 10a. (b) ScS δt measurements for those S-ScS pairs for which S source-side splitting is null. Plotting conventions are as in panel (a). (c) Histogram of ScS δt measurements obtained after correcting for source-side anisotropy inferred from S for those S-ScS pairs for which ScS polarizations are as predicted from S (under the assumption of a sign-flip of the radial component of ScS through the CMB reflection). Plotting conventions are as in panel (a).

328 shear wave splitting; however, the receiver-side corrections remain to be explored. We next use a realistic synthetic
 329 setup to test the accuracy of receiver-side corrections. We again incorporate olivine A-type (Figure 1c) anisotropy
 330 in the upper mantle and infer upper mantle shear wave splitting parameters from the SKS seismic phase recorded
 331 at an epicentral distance of 100° . We fit a $\sin(2\theta)$ -curve to the SKS SI values as a function of backazimuth, as com-
 332 monly done for real data (e.g., Chevrot, 2000; Monteiller and Chevrot, 2010). These results are shown in Figure 12a.
 333 The determined best-fitting splitting parameters are then used to correct ScS for the effect of anisotropy beneath the
 334 receiver for simulations that only include upper mantle receiver-side anisotropy. For approximately 40 % of robust
 335 ScS measurements (for the setup shown in Figure 1) the measured splitting is null (Figure 12b), as expected. For the
 336 remaining 60 % of robust measurements, a variety of ϕ' and δt values are obtained (Figure 12b). This exercise demon-
 337 strates that explicit receiver-side corrections for upper mantle anisotropy beneath the receiver are likely unreliable
 338 in real data. The challenges are likely to be particularly given that splitting patterns as a function of backazimuth are
 339 often substantially more complicated than in this simple synthetic scenario.

340 An example of a robust (but artificial) ScS splitting measurement obtained after correcting for receiver-side anisotropy
 341 determined using SKS phases is shown in Figure 13. This particular case corresponds to a scenario in which the

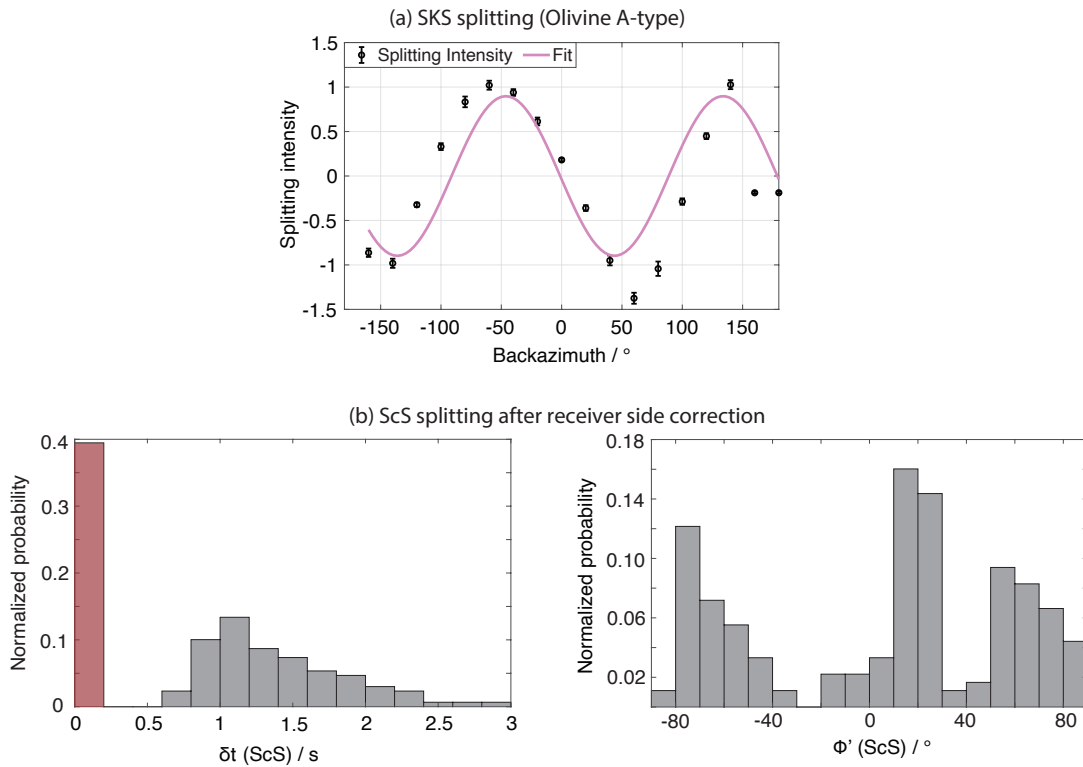


Figure 12 Apparent shear-wave splitting from ScS waveforms that were corrected for upper mantle anisotropy. (a) SKS SI values (black circles) and 95% confidence intervals (error bar) as a function of backazimuth. The fitted $\sin(2\theta)$ -curve to determine best-fitting splitting parameters is shown in pink. The best-fitting values are ($\phi = -1.2^\circ$, $\delta t = 0.9$ s). (b) ϕ' and δt histograms using the same plotting conventions as in Figure 10a.

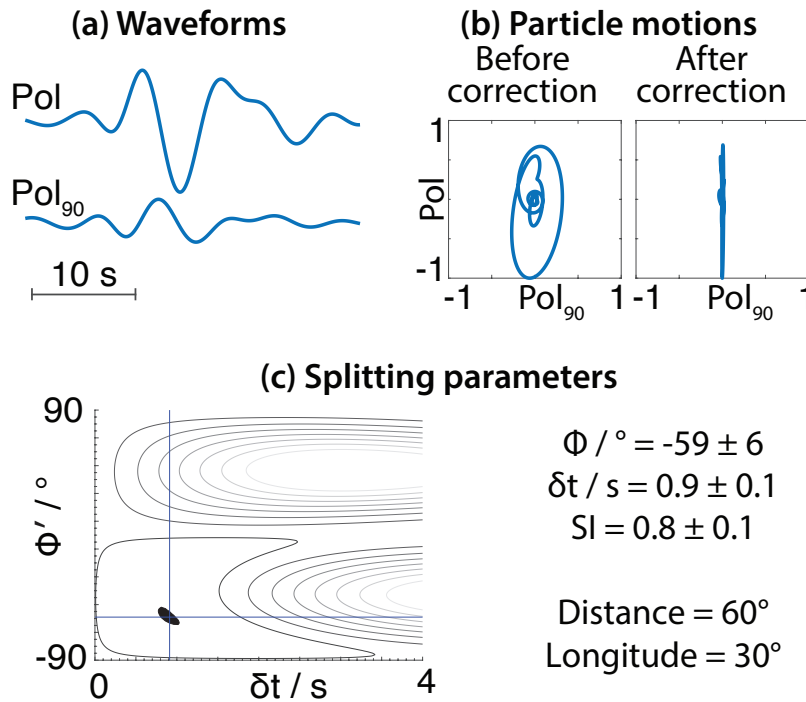


Figure 13 Measured shear wave splitting from waveforms corrected for upper mantle anisotropy inferred from SKS (Figure 12). Plotting conventions are identical to Figure 7.

342 olivine A-type elastic tensor is sampled from a backazimuth of 80° in Figure 12a. It is apparent that the $\sin(2\theta)$ -fit is
 343 imperfect for this backazimuth (Figure 12a), which is why the corrected waveform (Figure 13a) appears substantially
 344 split, the particle motion (Figure 13b) mimics splitting, and splitting parameters are well-constrained with very tight
 345 uncertainty intervals (Figure 13c), despite the lack of D'' anisotropy in this simulation.

346 While we conduct these measurements for ScS in this work, our calculations are similarly applicable for the mea-
 347 surement of S splitting after correcting for receiver-side anisotropy inferred from SKS, which is commonly done
 348 to infer seismic anisotropy in the transition zone in subduction zones (e.g., Russo et al., 2010; Mohiuddin et al.,
 349 2015; Eakin et al., 2018). One potential way to deal with this challenge may be to correct for upper mantle splitting
 350 beneath the receiver determined using other phases measured at the same backazimuth, preferably for the same
 351 source-receiver configuration. However, this appears challenging for ScS distance between 60° and 70° , as there is
 352 no obvious additional phase that could be used for such an approach.

353 9 Discussion

354 9.1 How to infer D'' anisotropy from ScS splitting measurements

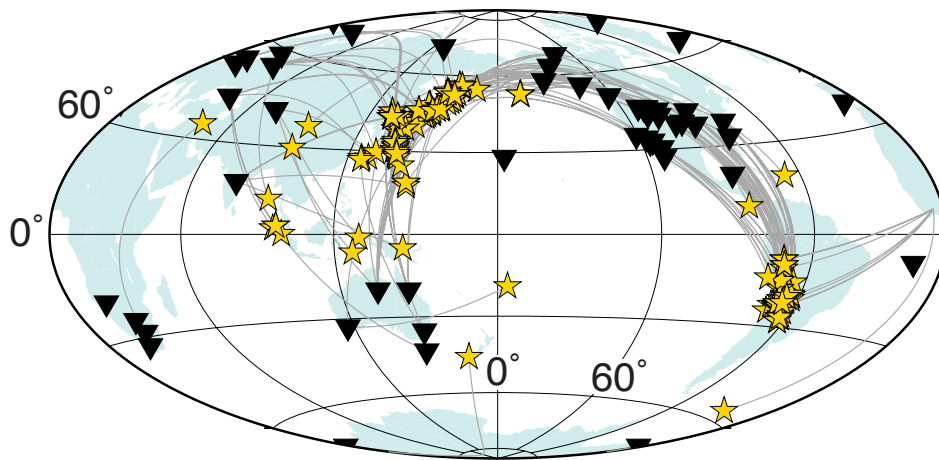


Figure 14 Source (yellow stars)-receiver (black triangles) configuration for global deep mantle anisotropy analysis using ScS. The selected stations are the null stations reported by Lynner and Long (2013) and Walpole et al. (2014). We only show sources for which well-constrained D'' anisotropy associated SI values could be obtained. Great circle raypaths are shown as gray lines.

355 We have shown that D'' anisotropy is challenging to infer from ScS waves that arrive at epicentral distances $<$
 356 60° , because CMB reflection coefficients for the SV component will strongly depend on the deep mantle velocity
 357 structure close to the ScS reflection point (Figure 3). Therefore, polarization directions of ScS, as well as apparent
 358 Pol/Pol_{90} amplitude ratios, will be influenced by effects other than seismic anisotropy. For epicentral distances
 359 between 70° and 80° , the ScS arrival may potentially be contaminated by (P)PS or SP (Figures 2 and 5), which strongly
 360 influences ScS polarizations (Figure 5). This can, in some cases, cause apparent ScS splitting in absence of seismic
 361 anisotropy (Figure 6c). For even larger distances, S and ScS merge (Figures 2, 4 and 5), which can lead to effects that
 362 mimic splitting, even for simple isotropic models such as isotropic PREM (Figure 6). Apparent splitting caused by
 363 isotropic effects at these distances can be indistinguishable from shear wave splitting caused by lowermost mantle
 364 anisotropy, with the waveform shape of the Pol_{90} component approximately agreeing with the time derivative of the
 365 Pol_0 component (Figure 7). Therefore, we suggest that ScS shear wave splitting measurements are difficult to reliably
 366 perform for epicentral distances $> 70^\circ$ and for most epicentral distances $< 60^\circ$ (with the exception, perhaps, of
 367 almost vertical incidence angles for small distances).

368 In the candidate epicentral distance range between 60° and 70° for ScS splitting measurements, the receiver- and
 369 source-side anisotropy influence is often explicitly corrected to extract the lowermost mantle contribution. However,

we have shown that explicit upper mantle anisotropy corrections can be unreliable (Figures 10 to 13) and therefore recommend only using ScS waves for which both source-side and receiver-side anisotropy are null. Practically, this means that ScS splitting measurements should only be applied at null stations for S-ScS pairs for which S source-side splitting is null. While these precautions mean that a much smaller number of S-ScS pairs are available for D'' splitting studies, they are likely to result in significantly higher-quality estimates of ScS splitting due to lowermost mantle anisotropy.

9.2 Global measurements of ScS splitting due to deep mantle anisotropy

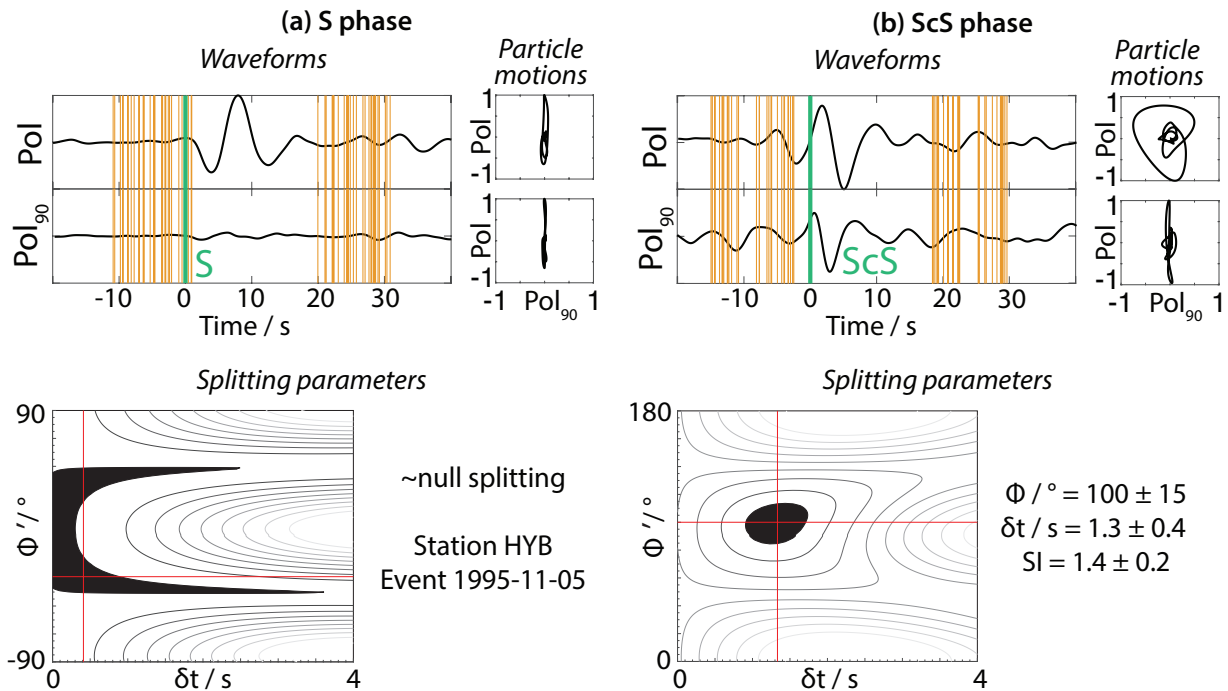


Figure 15 Example of an S and ScS splitting pair used to infer deep mantle anisotropy at station HYB for an event of 1995-11-05. (a) S Pol and Pol_{90} component velocity waveforms (top left). The PREM-predicted phase arrival time is shown by a light green line and the start/end of the automatically selected measurement windows are shown as orange lines. At the right we show S particle motions before (top) and after (bottom) correcting for the best fitting splitting parameters. At bottom, we show the best fitting splitting parameters for S in the ϕ' - δt plane. The 95% confidence interval is shown in black. Splitting for this S arrival is null. (b) Same as panel (a) for the corresponding ScS phase. ScS splitting parameters are shown in the bottom right.

We apply our strategy for estimating D''-associated ScS splitting measurements worldwide at the null stations reported by Lynner and Long (2013) and Walpole et al. (2014). We use all seismic events with moment magnitude > 5.7 in an epicentral distance range between 60° and 70° that occurred after January 1, 1990. The raypath coverage for all source-receiver pairs for which we could obtain well-constrained ScS splitting measurements is shown in Figure 14. Following the recommendations developed here, we only interpret ScS splitting as being indicative of deep mantle anisotropy if the S phase for the same source-receiver pair is not split. An example splitting measurement for such a S-ScS pair is presented in Figure 15.

We follow our suggested procedure to calculate splitting parameters to all our seismic data for null stations. All ScS splitting measurements due to lowermost mantle anisotropy are shown in map view in Figure 16. In some cases only well-constrained splitting intensities can be obtained. In other cases, splitting parameters (ϕ' , δt) can also be reliably measured. We can identify four different deep mantle regions A-D that show at least some evidence for

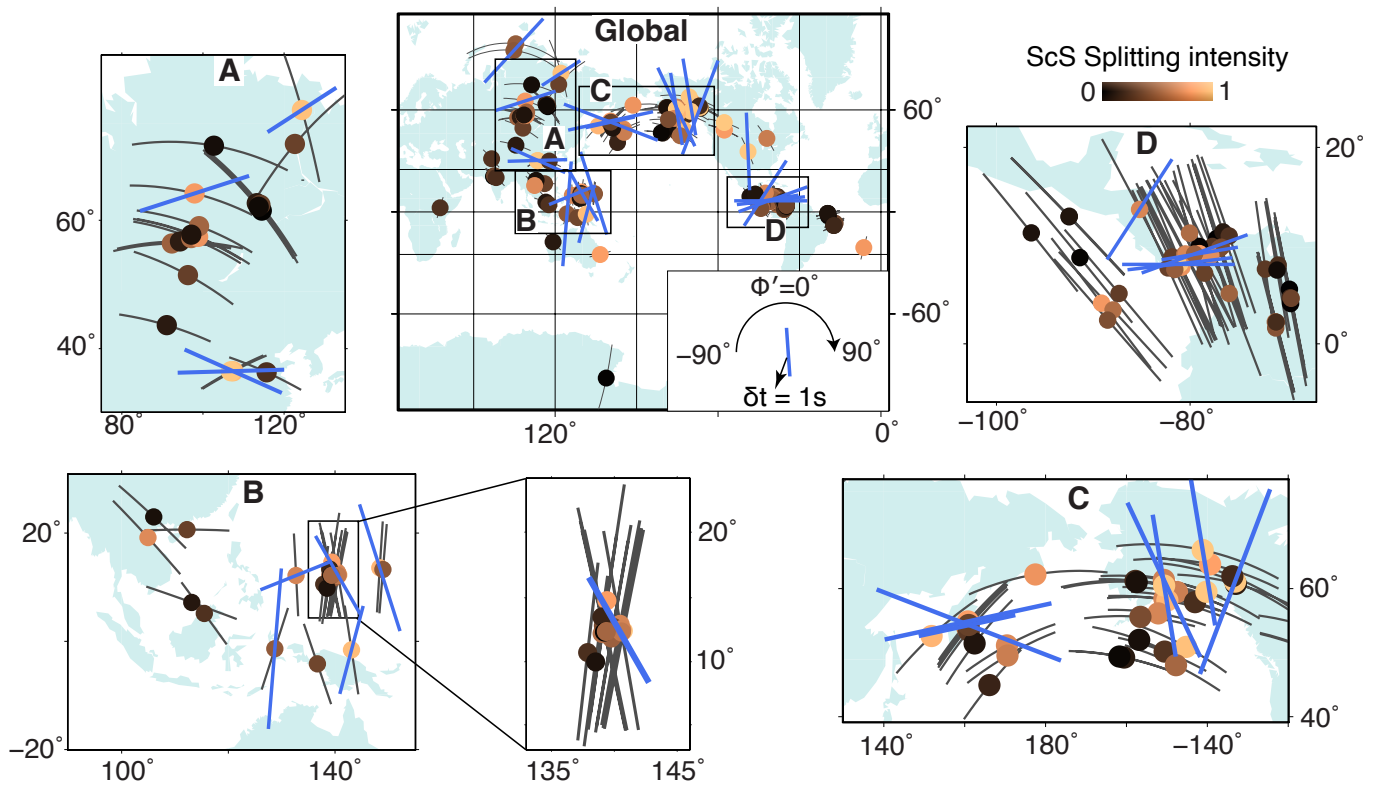


Figure 16 ScS splitting results for S-ScS pairs measured for station-event pairs shown in Figure 15, for which S splitting is null. Top center: Global results. ScS great circle raypaths through the lowermost 250 km of the mantle are shown as dark gray lines. Well-constrained ScS splitting intensity values are shown as colored circles (legend) at the ScS reflection point at the CMB. Splitting parameters (ϕ' , δt ; see legend) are shown as blue sticks and centered at the ScS reflection location. Different regions A-D with many well-constrained measurements are identified and labeled. Zoom-ins to these regions are shown in panels A-D surrounding the central plot.

388 anisotropy (Figure 16). Overall, we find evidence for seismic anisotropy in all regions in which ray coverage is good,
 389 suggesting that lowermost mantle anisotropy is likely widespread. These regions include central Asia (A), southeast
 390 Asia (B), northeast Russia/Alaska (C), and the Caribbean (D). North of region A, multiple studies have previously
 391 reported seismic anisotropy in D'' (e.g., Wookey and Kendall, 2008; Creasy et al., 2021). Our results for this raypath
 392 corridor approximately agree with the ϕ' values of 35° reported by Creasy et al. (2021) but are different than those
 393 from Wookey and Kendall (2008), who reported $\phi' \approx -7^\circ$. However, as mentioned above, ϕ' values depend on the
 394 initial polarization of the ScS wave, which is why we cannot necessarily expect to obtain the same ϕ' values for a
 395 particular region if the ScS initial polarizations in the dataset vary. Grund and Ritter (2018), Thomas and Kendall
 396 (2002) and Wolf et al. (2022b) also identified lowermost mantle anisotropy in some parts of region A using a different
 397 methodology. These measurements are hard to directly compare with ours; however, these studies are consistent
 398 with our finding of D'' anisotropy here.

399 Deep mantle anisotropy in region B has not been previously studied. We find the lowermost mantle in this region
 400 to be generally anisotropic; however, the strength of splitting due to seismic anisotropy varies (Figure 16). ϕ' -values
 401 tend to be close to 0° in most cases, but this – on its own – is an insufficient constraint on the geometry of anisotropy
 402 without taking into account the wave's initial polarization. The ScS raypaths through D'' , shown in the inset for region
 403 B (Figure 16), are close to the edge of the Pacific LLVP and show evidence for seismic anisotropy. This agrees with the
 404 finding of other studies that seismic anisotropy is often strong close to such edges (e.g., Wang and Wen, 2004; Lynner

405 and Long; 2014; Deng et al., 2017, Reiss et al.; 2019; Wolf and Long; 2023).

406 Much of region C has been found to be anisotropic in previous studies (e.g., Wookey et al., 2005; Asplet et al.,
407 2020, 2023; Suzuki et al., 2021; Wolf and Long; 2022; Wolf et al., 2023a; 2024). Direct comparisons to many of these
408 studies are difficult because they used different methods to infer the presence of seismic anisotropy. Wookey et al.
409 (2005) used S-ScS differential splitting to investigate the west portion of region C. Additionally, seismic anisotropy
410 has been detected in the western part of region C using multiple different methods (e.g., Wolf and Long, 2022; Asplet
411 et al., 2023), which include S-ScS and SKS-SKKS differential splitting as well as S_{diff} splitting. Notably, we also detect
412 particularly strong seismic anisotropy in this region.

413 Seismic anisotropy in region D has been identified by a large number of previous studies (e.g., Kendall and Sil-
414 ver, 1996; Rokosky et al., 2004, 2006; Garnero et al., 2004; Maupin et al., 2005; Nowacki et al., 2010). The study
415 by Nowacki et al. (2010) also used S-ScS differential splitting measurements. Interestingly, we find splitting due to
416 seismic anisotropy to be strong beneath central America and almost absent further to the east (Figure 16). In the
417 northwest part of region D, shear wave splitting is weak as well, while it is substantially stronger in the southwest
418 (Figure 16). To the east of region D we obtain five measurements that consistently show no evidence for splitting due
419 to deep mantle anisotropy, and whose initial polarizations differ by up to 40° . Therefore, we find the deep mantle in
420 this region to likely be isotropic, in disagreement with the findings of Pisconti et al. (2023).

421 Due to the constraints that we impose in our approach to the measurement of ScS splitting, a large majority of
422 seismograms cannot be used to reliably measure ScS splitting due to lowermost mantle anisotropy. A back-of-the-
423 envelope calculation suggests that approximately 15 million three-component seismograms are currently publicly
424 available for seismic events with moment magnitudes over 6.0. In this work, we obtain ~ 130 robust ScS splitting
425 measurements for seismic events with such moment magnitudes, using all null stations known to us (which may not
426 be all that exist). Following this line of reasoning, under the constraints used in this study, only one out of every
427 100,000 seismograms is expected to yield a robust ScS splitting measurement of lowermost mantle anisotropy – a
428 very small minority of available data. However, with the suggestions we put forward in Section 10, it may be possible
429 increase this number.

430 **9.3 Interpretations of ScS splitting measurements due to deep mantle anisotropy**

431 Our work demonstrates that when multiple sets of splitting parameters (ϕ , δt) due to lowermost mantle anisotropy
432 can be estimated in a particular region, a significant spread of these values can be expected (Figure 8). The reason is
433 that the measured (ϕ , δt)-values do not only depend on the nature of deep mantle anisotropy but also on the initial
434 polarization of ScS. Therefore, the measurement scatter shown in Figure 16 does not imply that measurements are
435 unreliable because displaying measurements in map projection does not account for the wave's initial polarization.
436 In fact, all SI measurements that are plotted on top of each other in Figure 16 and whose SI values differ have at least
437 somewhat different initial polarizations. In order to thoroughly characterize the geometry of deep mantle seismic
438 anisotropy measured from ScS waves, a sufficient number of splitting measurements is needed to allow for forward
439 modeling or inversions that explicitly consider the initial polarization of each wave. Practically, a sufficient number
440 of measurements may be difficult to obtain in many regions, given the substantial restrictions imposed to correctly
441 account for potential upper mantle contributions.

One potential way to make use of ScS splitting measurements to constrain the geometry of anisotropy as opposed to merely using them as an anisotropy detector is to interpret them along with other independent constraints, such as SKS-SKKS differential splitting (e.g., [Asplet et al., 2023](#)), D'' reflection polarities (e.g., [Pisconti et al., 2023](#)) or S_{diff} splitting (e.g., [Wolf et al., 2023b](#)). When multiple constraints are available, ray-theoretical forward modeling (e.g., [Wolf et al., 2019](#); [Pisconti et al., 2023](#)), full-wave simulations (e.g., [Wolf et al., 2022a](#); [2022b](#)), or inversions of ScS waveforms ([Asplet et al., 2023](#)) can potentially shed light on deformation in the deep mantle.

10 Ways forward

We have shown that it can be difficult to infer deep mantle anisotropy from ScS splitting measurements due to potential contamination from upper mantle anisotropy, which is difficult to account for. We have suggested a strategy of avoiding explicit upper mantle anisotropy corrections going forward by focusing on null stations and S-ScS pairs for which S is not split due to source-side upper mantle anisotropy. Crucial for this approach will be the identification of more null stations worldwide. In this work, we have used the null stations identified by [Lynner and Long \(2013\)](#) and [Walpole et al. \(2014\)](#); however, more null stations likely exist. Given the increased availability of seismic data since these two studies were published, it appears worthwhile to automatically and uniformly analyze all available broadband data to search for null stations, for example using an approach similar to [Walpole et al. \(2014\)](#).

Another possibility to increase the number of ScS splitting measurements due to deep mantle anisotropy is to use beamforming, which has only recently been applied in shear wave splitting studies ([Wolf et al., 2023a](#)). It has been shown that a beamforming approach effectively averages the upper mantle anisotropy contribution across the individual stations used to construct the beam ([Wolf et al., 2023a](#)). Therefore, it is possible to intentionally select stations such that the upper mantle anisotropy contribution to the beam beneath the array on the receiver side is effectively null. For such a station configuration, ScS splitting can be measured if the corresponding S beam splitting for the same source-array combination is null, indicating the absence of source-side anisotropy.

Interpretations of ScS splitting results in terms of anisotropic geometry will continue to be challenging. For such interpretations, the initial polarization of ScS will have to be explicitly considered. This has effectively been done by [Asplet et al. \(2023\)](#) by ensuring that ScS polarizations (approximately) agree with the backazimuth (through analysis of particle motions), although they used explicit upper mantle anisotropy corrections in their approach. At least in theory one could even go further: Seismic anisotropy in the lowermost mantle could be characterized by analyzing splitting intensities as a function of initial polarization for waves that sample the same lowermost mantle portion. However, given that we are dealing with two-layer splitting, this requires a much larger number of measurements than we have obtained for any particular region in this study (Figure 16). Most previous studies have not explicitly taken into account the ScS polarization and operated under the assumption that splitting due to D'' anisotropy should lead to the same $(\phi', \delta t)$ values for the same region and sampling direction (e.g., [Creasy et al., 2017](#); [Wolf et al., 2019](#); [Pisconti et al., 2023](#)).

If a sufficient number of ScS splitting measurements from earthquakes with different initial source polarizations can be obtained for a given set of raypaths sampling D'' , a two-layer inversion for splitting parameters on the down- and upgoing leg of the raypath appears promising. Such an approach can be applied analogously to two-layer split-

ting analysis for the upper mantle (e.g., [Silver and Savage, 1994](#); [Wolfe and Silver, 1998](#); [Aragon et al., 2017](#); [Link et al., 2022](#)). In our study, unfortunately, the number of well-constrained (ϕ , δt) measurements in any particular region is insufficient for the implementation of such an approach. As mentioned above, *SI* scattering is often straightforward to explain by different initial polarizations; in contrast, a precise characterization of the seismic anisotropy is challenging unless a large number of *SI* values for the same region can be obtained. Much easier is the detection of isotropic regions through initial polarization analysis, such as the isotropic region east of region D. The reason is that no more than a handful of null measurements with mutually different initial polarizations need to be obtained for the reliable characterization of an isotropic lowermost mantle region.

Going forward, it will also be important to combine ScS constraints with constraints from other seismic phases, whether waveform inversions (e.g., [Asplet et al., 2023](#)) or ray-theoretical forward modeling (e.g., [Suzuki et al., 2021](#); [Ford et al., 2015](#); [Wolf et al., 2019](#); [Pisconti et al., 2023](#)) approaches are used. Given the issues that have been pointed out with the use of ray-theoretical assumptions ([Nowacki and Wookey, 2016](#); [Wolf et al., 2022a](#)), it will be preferable to move away from ray-theory in future studies and make use of available full-wave modeling tools, including AxiSEM3D.

11 Conclusions

Using global wavefield simulations and calculations of ScS reflection coefficients, we have explored how ScS polarizations are affected by the CMB reflection. We find that measured ScS polarizations at the receiver, depend not only on the initial source polarization, but also on the deep mantle velocity structure at the reflection point and on the epicentral distance under consideration. In particular, in the epicentral distance between 60° and 70° , the CMB reflection can be well approximated as a sign-flip of SV, while SH is unaltered. For distances close than 60° , SV amplitudes are affected by the reflection, and for distances above 70° , apparent shear wave splitting can be introduced for isotropic input models due to phase interference, for example with S. Therefore the distance range suitable for ScS splitting measurements is 60° to 70° .

If ScS shear wave splitting is caused by lowermost mantle anisotropy, the measured apparent splitting parameters are substantially influenced by the initial source polarization of the wave. The reason is that each leg of the ScS raypath through D'' (downgoing and upgoing) experience splitting separately. Therefore, for any D'' region that is sampled from the same direction by multiple ScS waves, we would expect to measure a range of apparent splitting parameters that depend on the initial polarizations of the ScS waves. We have shown that if an anisotropy contribution on the source side is inferred from S splitting and then used to correct the ScS waveform, in many cases apparent D'' splitting can be introduced. Similar issues exist for explicit receiver-side corrections. Therefore, we suggest a strategy that only uses null stations to infer deep mantle anisotropy from ScS. Measurements of ScS splitting at null stations should only be attributed to deep mantle anisotropy if the measured S splitting for the same source-receiver pair is null. We have applied this analysis strategy globally and detected deep mantle seismic anisotropy in multiple regions around the Earth, including regions that have not been shown to be anisotropic before, for example, southern Russia and the southwestern Pacific Ocean.

Going forward, to improve D'' anisotropy sampling using ScS, the identification of more null stations and the

514 implementation of beamforming approaches in terms of the geometry of anisotropy will be helpful. Interpretations
515 of ScS splitting going beyond using ScS as a simple anisotropy detector will need to consider the initial polarization
516 of each ScS wave as well as potentially different splitting on the two ScS raypath legs through D'' . While this approach
517 is not typically incorporated in ScS splitting studies at present, it holds promise for gaining insight into the geometry
518 of the anisotropy, and thus flow at the base of the mantle.

519 **Acknowledgements**

520 This work was funded by Yale University and by the U.S. National Science Foundation via grant EAR-2026917 to MDL.
521 We thank the Yale Center for Research Computing for providing the necessary research computing infrastructure for
522 this study. The Generic Mapping Tools (Wessel and Smith, 1998), ObsPy (Beyreuther et al., 2010), MSAT (Walker and
523 Wookey, 2012), SplitRacer (Reiss and Rumpker, 2017) and AxiSEM3D (Leng et al., 2016) were used in this research.
524 This research was inspired by discussions with Ed Garnero. We thank Sanne Cottaar and the editor, Lauren Waszek,
525 for constructive reviews.

526 **Data and code availability**

527 All data used in this study are publicly available through Earthscope (<http://service.iris.edu>), SCEDC ([http://service.-
scedc.caltech.edu](http://service.-
528 scedc.caltech.edu)), RESIF (<http://ws.resif.fr>) and GEOFON (<http://geofon.gfz-potsdam.de>) data centers. We used data
529 from USArray (IRIS Transportable Array, 2003) and data from networks AK (Alaska Earthquake Center, Univ. of
530 Alaska Fairbanks, 1987), AT (NOAA National Oceanic and Atmospheric Administration (USA), 1967), CI (California In-
531 stitute of Technology and United States Geological Survey Pasadena, 1926), CN (Canada, 1975), G (Institut de physique
532 du globe de Paris (IPGP) and École et Observatoire des Sciences de la Terre de Strasbourg (EOST), 1982), GE (GEOFON
533 Data Centre, 1993), GT (Albuquerque Seismological Laboratory (ASL)/USGS, 1993), II (Scripps Institution of Oceanog-
534 raphy, 1986), IU (Albuquerque Seismological Laboratory/USGS, 2014), NL (KNMI, 1993), NR (Utrecht University (UU
535 Netherlands), 1983), PM (Instituto Português do Mar e da Atmosfera, I.P., 2006), IU (Albuquerque Seismological Lab-
536 oratory/USGS, 2014). The synthetic seismograms for this study were computed using AxiSEM3D, which is publicly
537 available at <https://github.com/AxiSEMunity> (Fernando et al., 2024).

538 **Competing interests**

539 The authors declare no competing interests with respect to this manuscript.

540 **References**

- 541 Alaska Earthquake Center, Univ. of Alaska Fairbanks. Alaska Geophysical Network, 1987. doi: 10.7914/SN/AK.
542 Albuquerque Seismological Laboratory (ASL)/USGS. Global Telemetered Seismograph Network (USAF/USGS), 1993. doi: 10.7914/SN/GT.
543 Albuquerque Seismological Laboratory/USGS. Global Seismograph Network (GSN - IRIS/USGS), 2014. doi: 10.7914/SN/IU.
544 Aragon, J. C., Long, M. D., and Benoit, M. H. Lateral Variations in SKS Splitting Across the MAGIC Array, Central Appalachians. *Geochemistry,
545 Geophysics, Geosystems*, 18:4136–4155, 2017.

- 546 Asplet, J., Wookey, J., and Kendall, M. A potential post-perovskite province in D'' beneath the Eastern Pacific: evidence from new analysis
547 of discrepant SKS–SKKS shear-wave splitting. *Geophysical Journal International*, 221:2075–2090, 2020. doi: 10.1093/gji/ggaa114.
- 548 Asplet, J., Wookey, J., and Kendall, M. Inversion of shear wave waveforms reveal deformation in the lowermost mantle. *Geophysical Journal
549 International*, 232:97–114, 2023. doi: 10.1093/gji/ggac328.
- 550 Barruol, G. and Kern, H. Seismic anisotropy and shear-wave splitting in lower-crustal and upper-mantle rocks from the Ivrea Zone: experi-
551 mental and calculated data. *Physics of the Earth and Planetary Interiors*, 95:175–194, 1996. doi: 10.1016/0031-9201(95)03124-3.
- 552 Beyreuther, M., Barsch, R., Krischer, L., Megies, T., Behr, Y., and Wassermann, J. ObsPy: A Python Toolbox for Seismology. *Seismological
553 Research Letters*, 81:530–533, 06 2010. doi: 10.1111/10.1785/gssrl.81.3.530.
- 554 Borgeaud, A. F., Konishi, K., Kawai, K., and Geller, R. J. Finite frequency effects on apparent S-wave splitting in the D'' layer: comparison
555 between ray theory and full-wave synthetics. *Geophysical Journal International*, 207:12–28, 2016. doi: 10.1093/gji/ggw254.
- 556 California Institute of Technology and United States Geological Survey Pasadena. Southern California Seismic Network, 1926.
557 doi: 10.7914/SN/CI.
- 558 Canada), N. R. C. N. Canadian National Seismograph Network, 1975. doi: 10.7914/SN/CN.
- 559 Chang, S.-J. and Ferreira, A. M. G. Inference on Water Content in the Mantle Transition Zone Near Subducted Slabs From Anisotropy Tomog-
560 raphy. *Geochemistry, Geophysics, Geosystems*, 20:1189–1201, 2019. doi: 10.1029/2018GC008090.
- 561 Chang, S.-J., Ferreira, A. M. G., Ritsema, J., van Heijst, H. J., and Woodhouse, J. H. Joint inversion for global isotropic and radially anisotropic
562 mantle structure including crustal thickness perturbations. *Journal of Geophysical Research: Solid Earth*, 120(6):4278–4300, 2015.
563 doi: 10.1002/2014JB011824.
- 564 Chapman, C. *Fundamentals of Seismic Wave Propagation*. Cambridge University Press, 2004. doi: 10.1017/CBO9780511616877.
- 565 Chevrot, S. Multichannel analysis of shear wave splitting. *Journal of Geophysical Research: Solid Earth*, 105:21579–21590, 2000.
566 doi: 10.1029/2000JB900199.
- 567 Cottaar, S. and Romanowicz, B. Observations of changing anisotropy across the southern margin of the African LLSVP. *Geophysical Journal
568 International*, 195:1184–1195, 2013. doi: 10.1093/gji/ggt285.
- 569 Creasy, N., Long, M. D., and Ford, H. A. Deformation in the lowermost mantle beneath Australia from observations and models of seismic
570 anisotropy. *Journal of Geophysical Research: Solid Earth*, 122:5243–5267, 2017. doi: 10.1002/2016JB013901.
- 571 Creasy, N., Miyagi, L., and Long, M. D. A Library of Elastic Tensors for Lowermost Mantle Seismic Anisotropy Studies and Comparison With
572 Seismic Observations. *Geochemistry, Geophysics, Geosystems*, 21:e2019GC008883, 2020. doi: 10.1029/2019GC008883.
- 573 Creasy, N., Pisconti, A., Long, M. D., and Thomas, C. Modeling of Seismic Anisotropy Observations Reveals Plausible Lowermost Mantle
574 Flow Directions Beneath Siberia. *Geochemistry, Geophysics, Geosystems*, 22(10):e2021GC009924, 2021. doi: 10.1029/2021GC009924.
- 575 Deng, J., Long, M. D., Creasy, N., Wagner, L., Beck, S., Zandt, G., Tavera, H., and Minaya, E. Lowermost mantle anisotropy near the eastern
576 edge of the Pacific LLSVP: constraints from SKS–SKKS splitting intensity measurements. *Geophysical Journal International*, 210:774–786,
577 2017. doi: 10.1093/gji/ggx190.
- 578 Dziewonski, A. M. and Anderson, D. L. Preliminary reference Earth model. *Physics of the Earth and Planetary Interiors*, 25:297–356, 1981.
579 doi: 10.1016/0031-9201(81)90046-7.
- 580 Eakin, C., Rychert, C., and Harmon, N. The Role of Oceanic Transform Faults in Seafloor Spreading: A Global Perspective From Seismic
581 Anisotropy. *Journal of Geophysical Research: Solid Earth*, 123:1736–1751, 2018.
- 582 Fernando, B., Wolf, J., Leng, K., Nissen-Meyer, T., Eaton, W., Styczinski, M., Walker, A., Craig, T., Muir, J., Nunn, C., and Long, M. AxiSEM3D -
583 an introduction to using the code and its applications. *EarthArXiv*, 2024. doi: 10.31223/X5TH7P.

- 584 Foley, B. J. and Long, M. D. Upper and mid-mantle anisotropy beneath the Tonga slab. *Geophysical Research Letters*, 38, 2011.
585 doi: 10.1029/2010GL046021.
- 586 Ford, H. A., Long, M. D., He, X., and Lynner, C. Lowermost mantle flow at the eastern edge of the African Large Low Shear Velocity Province.
587 *Earth and Planetary Science Letters*, 420:12–22, 2015. doi: 10.1016/j.epsl.2015.03.029.
- 588 Fouch, M. J., Fischer, K. M., and Wysession, M. E. Lowermost mantle anisotropy beneath the Pacific: Imaging the source of the Hawaiian
589 plume. *Earth and Planetary Science Letters*, 190(3):167–180, 2001. doi: 10.1016/S0012-821X(01)00380-6.
- 590 French, S. W. and Romanowicz, B. A. Whole-mantle radially anisotropic shear velocity structure from spectral-element waveform tomog-
591 raphy. *Geophysical Journal International*, 199(3):1303–1327, 2014. doi: 10.1093/gji/ggu334.
- 592 Garnero, E. J. and Lay, T. Lateral variations in lowermost mantle shear wave anisotropy beneath the north Pacific and Alaska. *Journal of*
593 *Geophysical Research: Solid Earth*, 102(B4):8121–8135, 1997. doi: 10.1029/96JB03830.
- 594 Garnero, E. J., Maupin, V., Lay, T., and Fouch, M. J. Variable Azimuthal Anisotropy in Earth's Lowermost Mantle. *Science*, 306(5694):259–261,
595 2004. doi: 10.1126/science.1103411.
- 596 GEOFON Data Centre. GEOFON Seismic Network, 1993. doi: 10.14470/TR560404.
- 597 Grund, M. and Ritter, J. R. Widespread seismic anisotropy in Earth's lowermost mantle beneath the Atlantic and Siberia. *Geology*, 47:
598 123–126, 2018. doi: 10.1130/G45514.1.
- 599 Haws, A. A., Long, M. D., and Luo, Y. Anisotropic structure of the normally-dipping and flat slab segments of the Alaska subduction zone:
600 Insights from receiver function analysis. *Tectonophysics*, 868:230112, 2023. doi: 10.1016/j.tecto.2023.230112.
- 601 Institut de physique du globe de Paris (IPGP) and École et Observatoire des Sciences de la Terre de Strasbourg (EOST). GEOSCOPE, French
602 Global Network of broad band seismic stations, 1982. doi: 10.18715/GEOSCOPE.G.
- 603 Instituto Português do Mar e da Atmosfera, I.P. Portuguese National Seismic Network, 2006. doi: 10.7914/SN/PM.
- 604 IRIS Transportable Array. USArray Transportable Array, 2003. doi: 10.7914/SN/TA.
- 605 Karato, S.-i. *Deformation of Earth Materials: An Introduction to the Rheology of Solid Earth*. Cambridge University Press, 2008.
606 doi: 10.1017/CBO9780511804892.
- 607 Kendall, J.-M. and Silver, P. Constraints from seismic anisotropy on the nature of the lower mantle. *Nature*, 381:409–412, 1996.
608 doi: 10.1038/381409a0.
- 609 KNMI. Netherlands Seismic and Acoustic Network, 1993. doi: 10.21944/E970FD34-23B9-3411-B366-E4F72877D2C5.
- 610 Komatitsch, D., Vinnik, L. P., and Chevrot, S. SHdiff-SVdiff splitting in an isotropic Earth. *Journal of Geophysical Research: Solid Earth*, 115
611 (B7), 2010. doi: 10.1029/2009JB006795.
- 612 Leng, K., Nissen-Meyer, T., and van Driel, M. Efficient global wave propagation adapted to 3-D structural complexity: a
613 pseudospectral/spectral-element approach. *Geophysical Journal International*, 207(3):1700–1721, 2016. doi: 10.1093/gji/ggw363.
- 614 Leng, K., Nissen-Meyer, T., van Driel, M., Hosseini, K., and Al-Attar, D. AxiSEM3D: broad-band seismic wavefields in 3-D global earth models
615 with undulating discontinuities. *Geophysical Journal International*, 217(3):2125–2146, 2019. doi: 10.1093/gji/ggz092.
- 616 Lin, Y.-P., Zhao, L., and Hung, S.-H. Full-wave effects on shear wave splitting. *Geophysical Research Letters*, 41:799–804, 2014.
617 doi: 10.1002/2013GL058742.
- 618 Link, F., Reiss, M. C., and Rumpker, G. An automatized XKS-splitting procedure for large data sets: Extension package for SplitRacer and
619 application to the USArray. *Computers & Geosciences*, 158:104961, 2022. doi: 10.1016/j.cageo.2021.104961.
- 620 Long, M. D. Complex anisotropy in D'' beneath the eastern Pacific from SKS–SKKS splitting discrepancies. *Earth and Planetary Science*

- 621 *Letters*, 283:181–189, 2009. doi: 10.1016/j.epsl.2009.04.019.
- 622 Long, M. D. and Becker, T. Mantle dynamics and seismic anisotropy. *Earth and Planetary Science Letters*, 297:341–354, 2010.
623 doi: 10.1016/j.epsl.2010.06.036.
- 624 Lynner, C. and Long, M. D. Sub-slab seismic anisotropy and mantle flow beneath the Caribbean and Scotia subduction zones: Effects of
625 slab morphology and kinematics. *Earth and Planetary Science Letters*, 361:367–378, 2013. doi: 10.1016/j.epsl.2012.11.007.
- 626 Lynner, C. and Long, M. D. Lowermost mantle anisotropy and deformation along the boundary of the African LLSVP. *Geophysical Research*
627 *Letters*, pages 3447–3454, 2014. doi: 10.1002/2014GL059875.
- 628 Lynner, C. and Long, M. D. Heterogeneous seismic anisotropy in the transition zone and uppermost lower mantle: evidence from South
629 America, Izu-Bonin and Japan. *Geophysical Journal International*, 201:1545–1552, 2015. doi: 10.1093/gji/ggv099.
- 630 Maupin, V., Garnero, E. J., Lay, T., and Fouch, M. J. Azimuthal anisotropy in the D'' layer beneath the Caribbean. *Journal of Geophysical*
631 *Research: Solid Earth*, 110(B8):B08301, 2005. doi: 10.1029/2004JB003506.
- 632 Mohiuddin, A., Long, M., and Lynner, C. Mid-mantle seismic anisotropy beneath Southwestern Pacific subduction systems and implica-
633 tions for mid-mantle deformation. *Physics of the Earth and Planetary Interiors*, 245, 2015. doi: 10.1016/j.pepi.2015.05.003.
- 634 Monteiller, V. and Chevrot, S. How to make robust splitting measurements for single-station analysis and three-dimensional imaging of
635 seismic anisotropy. *Geophysical Journal International*, 182:311–328, 2010. doi: 10.1111/j.1365-246X.2010.04608.x.
- 636 Nissen-Meyer, T., van Driel, M., Stähler, S. C., Hosseini, K., Hempel, S., Auer, L., Colombi, A., and Fournier, A. AxisSEM: broadband 3-D seismic
637 wavefields in axisymmetric media. *Solid Earth*, 5:425–445, 2014. doi: 10.5194/se-5-425-2014.
- 638 Niu, F. and Perez, A. M. Seismic anisotropy in the lower mantle: A comparison of waveform splitting of SKS and SKKS. *Geophysical Research*
639 *Letters*, 31, 2004. doi: 10.1029/2004GL021196.
- 640 NOAA National Oceanic and Atmospheric Administration (USA). National Tsunami Warning Center Alaska Seismic Network, 1967.
641 doi: 10.7914/SN/AT.
- 642 Nowacki, A. and Cottaar, S. *Toward Imaging Flow at the Base of the Mantle with Seismic, Mineral Physics, and Geodynamic Constraints*,
643 chapter 13, pages 329–352. American Geophysical Union (AGU), 2021. doi: 10.1002/9781119528609.ch13.
- 644 Nowacki, A. and Wookey, J. The limits of ray theory when measuring shear wave splitting in the lowermost mantle with ScS waves. *Geo-*
645 *physical Journal International*, 207:1573–1583, 2016. doi: 10.1093/gji/ggw358.
- 646 Nowacki, A., Wookey, J., and Kendall, J.-M. Deformation of the lowermost mantle from seismic anisotropy. *Nature*, 467:1091–1094, 2010.
647 doi: 10.1038/nature09507.
- 648 Panning, M. and Romanowicz, B. A three-dimensional radially anisotropic model of shear velocity in the whole mantle. *Geophysical Journal*
649 *International*, 167:361–379, 2006. doi: 10.1111/j.1365-246X.2006.03100.x.
- 650 Parisi, L., Ferreira, A. M. G., and Ritsema, J. Apparent Splitting of S Waves Propagating Through an Isotropic Lowermost Mantle. *Journal of*
651 *Geophysical Research: Solid Earth*, 123:3909–3922, 2018. doi: 10.1002/2017JB014394.
- 652 Pisconti, A., Creasy, N., Wookey, J., Long, M. D., and Thomas, C. Mineralogy, fabric and deformation domains in D'' across the southwestern
653 border of the African LLSVP. *Geophysical Journal International*, 232:705–724, 2023. doi: 10.1093/gji/ggac359.
- 654 Pulliam, J. and Sen, M. K. Seismic anisotropy in the core—mantle transition zone. *Geophysical Journal International*, 135:113–128, 1998.
655 doi: 10.1046/j.1365-246X.1998.00612.x.
- 656 Reiss, M. and Rumpker, G. SplitRacer: MATLAB Code and GUI for Semiautomated Analysis and Interpretation of Teleseismic Shear-Wave
657 Splitting. *Seismological Research Letters*, 88:392 – 409, 2017. doi: 10.1785/0220160191.

- 658 Reiss, M. C., Long, M. D., and Creasy, N. Lowermost Mantle Anisotropy Beneath Africa From Differential SKS-SKKS Shear-Wave Splitting.
659 *Journal of Geophysical Research: Solid Earth*, 124(8):8540–8564, 2019. doi: 10.1029/2018JB017160.
- 660 Ritsema, J., Deuss, A., van Heijst, H. J., and Woodhouse, J. H. S40RTS: a degree-40 shear-velocity model for the mantle from new Rayleigh
661 wave dispersion, teleseismic traveltimes and normal-mode splitting function measurements. *Geophysical Journal International*, 184(3):
662 1223–1236, 2011. doi: 10.1111/j.1365-246X.2010.04884.x.
- 663 Rokosky, J. M., Lay, T., Garnero, E. J., and Russell, S. A. High-resolution investigation of shear wave anisotropy in D'' beneath the Cocos
664 Plate. *Geophysical Research Letters*, 31:L07605, 2004. doi: 10.1029/2003GL018902.
- 665 Rokosky, J. M., Lay, T., and Garnero, E. J. Small-scale lateral variations in azimuthally anisotropic D'' structure beneath the Cocos Plate.
666 *Earth and Planetary Science Letters*, 248:411–425, 2006. doi: 10.1016/j.epsl.2006.06.005.
- 667 Russo, R., Gallego, A., Comte, D., Mocanu, V., Murdie, R., and VanDecar, J. Source-side shear wave splitting and upper mantle flow in the
668 Chile Ridge subduction Region. *Geology*, 38:707–710, 2010. doi: 10.1130/G30920.1.
- 669 Savage, M. K. Seismic anisotropy and mantle deformation: What have we learned from shear wave splitting? *Reviews of Geophysics*, 37:65
670 – 106, 1999. doi: 10.1016/10.1029/98RG02075.
- 671 Scripps Institution of Oceanography. Global Seismograph Network - IRIS/IDA, 1986. doi: 10.7914/SN/II.
- 672 Silver, P. G. Seismic Anisotropy beneath the Continents: Probing the Depths of Geology. *Annual Review of Earth and Planetary Sciences*, 24
673 (1):385 – 432, 1996. doi: 10.1146/annurev.earth.24.1.385.
- 674 Silver, P. G. and Chan, W. W. Shear wave splitting and subcontinental mantle deformation. *Journal of Geophysical Research: Solid Earth*, 96:
675 16429–16454, 1991. doi: 10.1029/91JB00899.
- 676 Silver, P. G. and Long, M. D. The non-commutivity of shear wave splitting operators at low frequencies and implications for anisotropy
677 tomography. *Geophysical Journal International*, 184(3):1415–1427, 2011. doi: 10.1111/j.1365-246X.2010.04927.x.
- 678 Silver, P. G. and Savage, M. K. The Interpretation of Shear-Wave Splitting Parameters In the Presence of Two Anisotropic Layers. *Geophysical*
679 *Journal International*, 119:949–963, 1994.
- 680 Suzuki, Y., Kawai, K., and Geller, R. J. Imaging paleoslabs and inferring the Clapeyron slope in D'' beneath the northern Pacific based on
681 high-resolution inversion of seismic waveforms for 3-D transversely isotropic structure. *Physics of the Earth and Planetary Interiors*, page
682 106751, 2021. doi: 10.1016/j.pepi.2021.106751.
- 683 Tesoniero, A., Leng, K., Long, M. D., and Nissen-Meyer, T. Full wave sensitivity of SK(K)S phases to arbitrary anisotropy in the upper and
684 lower mantle. *Geophysical Journal International*, 222(1):412 – 435, 2020. doi: 10.1093/gji/ggaa171.
- 685 Thomas, C. and Kendall, J.-M. The lowermost mantle beneath northern Asia—II. Evidence for lower-mantle anisotropy. *Geophysical Journal*
686 *International*, 151:296–308, 2002. doi: 10.1046/j.1365-246X.2002.01760.x.
- 687 Utrecht University (UU Netherlands). NARS, 1983. doi: 110.7914/SN/NR.
- 688 Walker, A. and Wookey, J. MSAT - a new toolkit for the analysis of elastic and seismic anisotropy. *Computers and Geosciences*, 49:81–90,
689 2012. doi: 10.1016/j.cageo.2012.05.031.
- 690 Walpole, J., Wookey, J., Masters, G., and Kendall, J. M. A uniformly processed data set of SKS shear wave splitting measurements: A
691 global investigation of upper mantle anisotropy beneath seismic stations. *Geochemistry, Geophysics, Geosystems*, 15:1991–2010, 2014.
692 doi: 10.1002/2014GC005278.
- 693 Walsh, E., Arnold, R., and Savage, M. K. Silver and Chan revisited. *Journal of Geophysical Research: Solid Earth*, 118:5500–5515, 2013.
694 doi: 10.1002/jgrb.50386.
- 695 Wang, Y. and Wen, L. Mapping the geometry and geographic distribution of a very low velocity province at the base of the Earth's mantle.

- 696 *Journal of Geophysical Research: Solid Earth*, 109, 2004. doi: 10.1029/2003JB002674.
- 697 Wessel, P. and Smith, W. H. F. New, improved version of generic mapping tools released. *Eos, Transactions American Geophysical Union*, 79:
698 579–579, 1998. doi: 10.1029/98EO00426.
- 699 Wolf, J. and Long, M. D. Slab-driven flow at the base of the mantle beneath the northeastern Pacific Ocean. *Earth and Planetary Science*
700 *Letters*, 594:117758, 2022. doi: 10.1016/j.epsl.2022.117758.
- 701 Wolf, J. and Long, M. D. Lowermost mantle structure beneath the central Pacific Ocean: Ultralow velocity zones and seismic anisotropy.
702 *Geochemistry, Geophysics, Geosystems*, 24:e2022GC010853, 2023. doi: 10.1029/2022GC010853.
- 703 Wolf, J., Creasy, N., Pisconti, A., Long, M. D., and Thomas, C. An investigation of seismic anisotropy in the lowermost mantle beneath Iceland.
704 *Geophysical Journal International*, 219(Supplement_1):S152 – S166, 2019. doi: 10.1093/gji/ggz312.
- 705 Wolf, J., Long, M. D., Leng, K., and Nissen-Meyer, T. Sensitivity of SK(K)S and ScS phases to heterogeneous anisotropy in the lowermost
706 mantle from global wavefield simulations. *Geophysical Journal International*, 228:366–386, 2022a. doi: 10.1093/gji/ggab347.
- 707 Wolf, J., Long, M. D., Leng, K., and Nissen-Meyer, T. Constraining deep mantle anisotropy with shear wave splitting measurements: Chal-
708 lenges and new measurement strategies. *Geophysical Journal International*, 230:507–527, 2022b. doi: 10.1093/gji/ggac055.
- 709 Wolf, J., Frost, D. A., Long, M. D., Garnero, E., Aderoju, A. O., Creasy, N., and Bozdağ, E. Observations of Mantle Seismic Anisotropy Using Array
710 Techniques: Shear-Wave Splitting of Beamformed SmKS Phases. *Journal of Geophysical Research: Solid Earth*, 128(1):e2022JB025556,
711 2023a. doi: 10.1029/2022JB025556.
- 712 Wolf, J., Long, M. D., Creasy, N., and Garnero, E. On the measurement of Sdiff splitting caused by lowermost mantle anisotropy. *Geophysical*
713 *Journal International*, 2023b. doi: 10.1093/gji/ggac490.
- 714 Wolf, J., Long, M. D., Li, M., and Garnero, E. Global Compilation of Deep Mantle Anisotropy Observations and Possible Correlation With Low
715 Velocity Provinces. *Geochemistry, Geophysics, Geosystems*, 24(10):e2023GC011070, 2023c.
- 716 Wolf, J., Li, M., Haws, A. A., and Long, M. D. Strong seismic anisotropy due to upwelling flow at the root of the Yellowstone mantle plume.
717 *Geology*, 2024. doi: 10.1130/G51919.1.
- 718 Wolf, J., Long, M. D., and Frost, D. A. Ultralow velocity zone and deep mantle flow beneath the Himalayas linked to subducted slab. *Nature*
719 *Geoscience*, pages 1–7, 2024. doi: 10.1038/s41561-024-01386-5.
- 720 Wolfe, C. J. and Silver, P. G. Seismic anisotropy of oceanic upper mantle: Shear wave splitting methodologies and observations. *Journal of*
721 *Geophysical Research: Solid Earth*, 103(B1):749–771, 1998. doi: 10.1029/97JB02023.
- 722 Wookey, J. and Kendall, J.-M. Constraints on lowermost mantle mineralogy and fabric beneath Siberia from seismic anisotropy. *Earth and*
723 *Planetary Science Letters*, 275:32–42, 2008. doi: 10.1016/j.epsl.2008.07.049.
- 724 Wookey, J., Kendall, J.-M., and Rumpker, G. Lowermost mantle anisotropy beneath the north Pacific from differential S-ScS splitting.
725 *Geophysical Journal International*, 161:829–838, 2005. doi: 10.1111/j.1365-246X.2005.02623.x.
- 726 Wookey, J., Stackhouse, S., Kendall, J.-M., Brodholt, J., and Price, G. Efficacy of the Post-Perovskite Phase as an Explanation for Lowermost-
727 Mantle Seismic Properties. *Nature*, 438:1004–1007, 2005b. doi: 10.1038/nature04345.
- 728 Yuan, K. and Beghein, C. Three-dimensional variations in Love and Rayleigh wave azimuthal anisotropy for the upper 800km of the mantle.
729 *Journal of Geophysical Research: Solid Earth*, 119:3232–3255, 2014. doi: 10.1002/2013JB010853.
- 730 Zhu, H., Yang, J., and Li, X. Azimuthal Anisotropy of the North American Upper Mantle Based on Full Waveform Inversion. *Journal of*
731 *Geophysical Research: Solid Earth*, 125(2):e2019JB018432, 2020. doi: 10.1029/2019JB018432.